The Planetary Science Journal, 5:254 (29pp), 2024 November https://doi.org/10.3847/PSJ/ad888d

Detection of Hydration on Nominally Anhydrous S-complex Main Belt Asteroids

Maggie McAdam[1], Cristina Thomas[2], Lauren McGraw[2], Andrew Rivkin[3], and Joshua Emery[2]
[1] NASA Ames Research Center, PO Box 1, Moffett Field, CA 94035, USA
[2] Northern Arizona University, DAPS: Room 209, Building 19, Physical Sciences, 527 S. Beaver Street, Flagstaff, AZ 86011, USA
[3] Johns Hopkins University's Applied Physics Laboratory, 11100 Johns Hopkins Road, Laurel, MD 20723, USA
Received 2023 July 21; revised 2024 July 30; accepted 2024 October 8; published 2024 November 25

Abstract

We present the results of a survey of nominally anhydrous main belt S-complex asteroids. Thirty-three observations of 29 unique asteroids were obtained using the IRTF+SpeX instrument in prism and LXD short modes. We report for the first time that S-complex main belt asteroids have 3 μm features. The majority of the observations (27 of 33) have a detectable 3 μm feature that has at least 1% band depth or greater (within error), indicating the presence of hydration. Most of the asteroids have bands of 1%–2.5% depth, but a notable fraction (nine of the observations) have band depths of >5%. These band depths are comparable to those of low albedo asteroids in the middle and outer belt that have experienced aqueous alteration. We investigate the origin of the hydration, searching for correlations with orbital, physical, and circumstantial parameters. However, we do not find any strong or moderate correlations with 3 μm band depth, indicating that multiple factors may be at play, including exogenic sources, primordial water, and/or solar wind implantation. Additionally, we report the mineralogies of the asteroids, derived from the prism observations.

Unified Astronomy Thesaurus concepts: Planetary science (1255); Asteroids (72); Infrared spectroscopy (2285)

1. Introduction

In our solar system, we observe two broadly defined regions characterized by the abundance of water: the icy outer solar system with less abundant rocky materials, and the inner solar system characterized by a greater abundance of rocky materials and less abundant volatiles, especially water. This is not to say that the inner solar system has no water, but rather that the water observed on planets and small bodies interior to Jupiter's orbit represents a much lower proportion of the materials compared to the outer solar system bodies like comets, trans-Neptunian objects, and icy moons.

Water is present on every planet in the inner solar system (e.g., T. M. Donahue & R. R. Hodges 1993; D. J. Lawrence et al. 2013; R. D. Wordsworth 2016; J. J. Wray 2021), including the Moon (e.g., R. N. Clark 2009; C. M. Pieters et al. 2009; J. M. Sunshine et al. 2009; C. I. Honniball et al. 2021, 2022). Water and hydroxyl found in the inner solar system may be formed in situ (e.g., C. I. Honniball et al. 2021), delivered to the surface (e.g., M. Benna et al. 2019), or created on the surface through interactions with the solar wind (e.g., C. A. Hibbitts et al. 2011). Evidence of water has also been observed on asteroids.

In the main asteroid belt, evidence of water ice and organics has been inferred by bowl-shaped 3 μm features (e.g., H. Campins et al. 2010; A. S. Rivkin & J. P. Emery 2010; D. Takir & J. P. Emery 2012). Other evidence of water has been seen on Ceres, which is thought to have experienced extensive interactions with coaccreted water (e.g., M. C. De Sanctis et al. 2020). Psyche and other M types have also been observed to have the signature of hydration around 3 μm (T. D. Jones et al. 1990; A. S. Rivkin et al. 2000; Z. A. Landsman et al. 2015). Similarly, remote observations of Vesta indicate the presence of a 3 μm band (e.g., S. Hasegawa et al. 2003; L. E. McGraw et al. 2022). Observations made by the Dawn mission indicate that the enhanced signature of hydrogen from gamma-ray neutron spectral observations is not merely caused by solar wind implantation (T. H. Prettyman et al. 2012). Dawn results also find evidence of dark exogenic material on Vesta's surface, which likely causes the weak 3 μm feature observed in Vesta's spectrum (e.g., S. Hasegawa et al. 2003; T. B. McCord et al. 2012; V. Reddy et al. 2012; L. E. McGraw et al. 2022). In near-Earth space, 3 μm features have been detected on Eros and Ganymed, two of the largest near-Earth objects (e.g., A. S. Rivkin et al. 2018). L. E. McGraw et al. (2022) also presented a survey of near-Earth asteroids showing more detections of 3 μm features that could be caused by implanted OH from solar wind or exogenic material similar to Vesta. Finally, Galileo observations of the S-type asteroid Gaspra also indicate the presence of hydration (e.g., J. C. Granahan et al. 1994; J. C. Granahan 2011).

Main belt S-complex asteroids, as a taxonomic class, have not been systematically observed to search for evidence of hydration (water ice, hydroxyl in hydrated minerals). In fact, S-complex asteroids have always been assumed to be dry, that is, that they do not contain water or at least contain a negligible abundance of water at the time of accretion. Without significant water at the time of accretion, S-complex asteroids do not have significant phyllosilicates like C-complex asteroids. S-complex asteroids are assumed to be dry because they formed in the inner solar system like the terrestrial planets (e.g., J. F. Bell et al. 1989; S. N. Raymond & D. Nesvorny 2022; R. Deienno et al. 2023; A. Izidoro et al. 2023). However, evidence in meteorites suggests that even anhydrous groups, including ordinary chondrites, have detectable water in them (e.g., J. A. Wood 2005). Given the observations from ordinary chondrites, which are thought to be linked to S-type asteroids, as well as the pervasive detection of hydration across many anhydrous asteroids, including Vesta and Psyche, we prepared

an investigation of S-complex asteroids searching for 3 μm features.

In this study, we investigate both the evidence of hydration, through 3 μm spectroscopy on nominally anhydrous inner and middle main belt S-type asteroids, and its potential origin. Here "hydration" is defined as the detection of a 3 μm feature that is produced by the fundamental vibration of O–H bonds in hydroxyl and/or water. In the 3 μm wavelength region, water (H_2O molecules) and hydroxyl (OH molecules) share a degenerate vibrational mode. We cannot distinguish between OH and H_2O using this wavelength region alone, but the presence of a 3 μm band is indicative of OH/H_2O. The signature of hydration can be caused by hydrated minerals (such as phyllosilicates) that are endogenic to the object, OH created on grain surfaces through interactions with solar wind, and/or exogenic hydrated minerals brought to an object through impacts.

We present a large study of 29 nominally anhydrous S-type asteroids using near-infrared spectral observations from NASA's Infrared Telescope Facility's SpeX instrument in the prism (0.7–2.5 μm) and LXD short (1.67–4.2 μm) modes to investigate whether these objects show the telltale hydration absorption in this region, as well as their underlying silicate mineralogy. This data set, representing hundreds of hours of observing time, is the starting place to investigate the pervasive presence of water throughout the main asteroid belt. We will present our data set and potential explanations for the hydration on these S-type asteroids.

2. Observations and Data Reduction

2.1. Observations

We were awarded 30 observing runs with IRTF between 2017 February and 2020 May. Over these nights, we obtained 34 observations of 29 unique S-type asteroids. We used the SpeX instrument (J. T. Rayner et al. 2003) for these observations in both the prism (0.7–2.52 μm, $R \sim 200$) and LXD short modes (1.67–4.2 μm, $R \sim 2500$). Our observations were made using the 0.8" slit. In general, we observed each object using the prism and LXD modes on the same night of observing. A few of the asteroids were only observed with the LXD mode, and one had a prism spectrum taken on a different night. Integration times, co-adds, and total exposure times were chosen based on the asteroid's brightness and the weather conditions. Particularly in prism mode, the exposure times vary owing to the brightness of the objects in this study. A summary of the asteroids, dates, observing circumstances, total exposure time, and standard stars are listed in Table 1.

Standard stars were selected in two ways. Often, we used Bobby Bus's standard-star list from SMASS observations (T. H. Burbine & R. P. Binzel 2002). Additionally, we searched for solar-like standard stars in the SIMBAD database within a 4° radius around the asteroid's position on the night of observation to ensure a good telluric match for the LXD reduction process. The closest G star in the sky with $B - V$ and $V - K$ colors most similar to the Sun was selected.

2.2. Reduction

2.2.1. Prism Data Reduction

After the data were collected, they were reduced using the IDL Spextool package (W. D. Vacca et al. 2003; M. C. Cushing et al. 2004). Each image was first extracted using Spextool. Telluric corrections were done with an ATRAN-based code (E. MacLennan 2019), and then the tellurically corrected data were combined into a single spectrum for analysis. The prism data and derived mineralogy are discussed in Section 4.1 and Appendix A, respectively.

2.2.2. LXD Data Reduction

The LXD spectra were extracted using Spextool, corrected for telluric contamination with the basic telluric correction package that divides by the contemporaneous standard-star observations, and then combined and merged into a single spectrum. We followed the process presented in L. E. McGraw et al. (2022) of frequent standard-star observations. This package provides flat-field correction and wavelength calibrations to extract the spectra. Standard stars and asteroids were extracted using the same process, and then the standards observed at similar air masses were used to remove telluric contamination. The data between 2.55 and 2.85 μm are excluded because the atmosphere is opaque in this region owing to the absorption of atmospheric water.

After first processing all of the data in this manner, we noted that several objects (11) had a persistent artifact in their spectra. This appeared as a bump around 3.5 μm. This feature is caused by the sensitivity drop-off at the edges of the LXD orders around 3.5 μm. As a consequence, the object-tracing algorithm failed to properly find the object's location in the slit during the initial extraction step. When the orders were subsequently merged, the 3.5 μm bump artifact appeared because there was not sufficient signal in the orders to adequately combine the data, resulting in the bump artifact. To solve this problem, we rereduced the asteroid data by first combining the images (which enhances the signal at all wavelengths) and then performing the flat field, wavelength calibrations, and extraction steps. Data were then tellurically corrected and merged to create a final spectrum used for analysis. When the spectra are combined first, there are sufficient signal-to-noise ratios in each order to allow the tracing algorithm to accurately find and trace the object in the slit.

2.3. Thermal Modeling

In the LXD wavelength region, asteroids exhibit a thermal excess caused by the blackbody reradiation of the asteroid itself. Depending on the temperature of the asteroid, the thermal excess can be significant and obscure underlying mineralogy and/or signature of hydration (if present) in the ~2.8–4.2 μm region. We utilize a thermal modeling code based on the Near-Earth Asteroid Thermal Model (A. W. Harris 1998) to remove the thermal excess.

The LXD spectra cover the K and L bands (2–2.4 μm and 3–4 μm, respectively). In the thermal model code, we assume that thermal excess is all in the K band (~2–2.5 μm) and L band (~3–4 μm). The thermal excess is then modeled based on the asteroid's phase angle, size, albedo, and relative position to the Sun (r_H) and Earth (Δ). We then subtract off combined thermal continuum, thus removing the contribution from the blackbody radiation of the asteroid. Figure 1 shows an example of a spectrum, thermal model, and thermally corrected data.

Separately, we also calculate the instantaneous theoretical equilibrium temperature of each object. We calculate this

Table 1
Observation Circumstances

Object	Date	Standard Star	LXD Midtime	Integration Time	No. Images	Prism Midtime	Integration Time	No. Images	Weather (Seeing) (arcsec)	r_H	Delta	Phase
3 Juno	11/17/2018	HD 23030	9:17	830	68	n.a.	n.a.	n.a.	not reported	1.98	1.04	11.27
5 Astrea	2/3/2020	HD 62346	12:15	300	40	11:08	24	8	0.64	2.09	1.13	7.48
6 Hebe	12/18/2018	HD 46055	14:20	960	64	15:24	180	36	0.5	2.20	1.26	9.99
7 Iris (2018-12-13)	12/13/2018	HD 109130	15:27	960	64	14:19	42	10	0.472	2.64	2.78	20.7
8 Flora	12/27/2017	HD 268518	11:55	240	32	n.a.	n.a.	n.a.	0.84	2.01	1.03	4.43
9 Metis	10/3/2019	BD+03 324	14:46	480	32	14:15	46	18	0.83 (intermittent fog)	2.18	1.24	12.6
11 Parthenope	5/14/2019	HD 140460	10:14	960	64	9:04	64	16	1.05	2.42	1.42	3.16
14 Irene (2019-10-03)	10/3/2019	HD 12356	12:56	660	64	13:50	140	16	0.83 (intermittent fog)	2.99	2.04	6.91
14 Irene (2020-02-03)	2/3/2020	HD 9595	6:39	1110	74	5:23	60	4	0.4	2.89	3.06	18.79
Irene (2017-02-15)	2/15/2017	HD 93215	12:02	630	52	10:33	24	16	not reported	2.21	1.24	6.76
17 Thetis (2018-12-16)	12/16/2018	HD 104770	14:43	420	56	13:50	240	8	0.68	2.51	2.41	22.93
17 Thetis (2019-03-15)	3/15/2019	BD+62574	12:44	960	64	11:32	15	10	0.632	2.38	1.40	4.96
18 Melpomene	7/4/2019	HD 172317	9:34	960	64	8:36	⋯	8	0.71	2.26	1.26	6.38
20 Massalia	12/27/2017	HD 35769	10:45	180	24	9:50	24	8	0.84	2.07	1.10	5.57
30 Urania	9/18/2018	SA 115271	11:01	930	62	9:59	60	10	clear	2.12	1.11	1.54
33 Polyhymnia	10/9/2019	HD 8233	9:08	630	42	⋯	111	18	0.67	1.99	0.99	3.4
39 Laetitia	8/26/2019	HD 202954	9:50	630	42	8:45	34	22	0.55	2.53	1.52	4.38
63 Ausonia	4/23/2017	HD 111546	9:37	1140	76	7:45	280	14	1	2.25	1.27	7.11
67 Asia	5/2/2019	HD 113763	7:18	720	80	5:38	120	8	1	2.43	1.46	8.96

Table 1
(Continued)

Object	Date	Standard Star	LXD Midtime	Integration Time	No. Images	Prism Midtime	Integration Time	No. Images	Weather (Seeing) (arcsec)	r_H	Delta	Phase
82 Alkmene	2/10/2017	BD+19 2241	11:55	180	86	10:15	110	12	0.65	2.16	1.18	2.14
103 Hera (2020-09-20)	9/20/2019	HD 225211	11:18	540	72	10:08	80	8	cloudy	2.52	1.51	2.34
115 Thyra (prism)	9/7/2018	HD 213275	n.a.	n.a.	n.a.	8:26	40	8	1.33	…	…	…
115 Thyra (LXD)	3/6/2020	HD 94723	10:10	1080	72	n.a.	n.a.	n.a.	0.8	2.55	1.57	4.6
151 Abunditia	3/15/2019	HD 104925	14:28	960	64	15:23	300	10	0.632	2.51	1.52	4.02
182 Elsa (2019-10-03)	9/26/2019	HD 472	8:52	960	64	7:10	240	16	0.83 (intermittent fog)	2.09	1.09	3.03
182 Elsa (2020-09-26)	10/3/2019	HD 2691	10:50	660	44	10:12	200	16	clear	2.10	1.10	2.43
208 Lacrimosa	2/17/2019	HD 87776	12:12	2400	160	10:00	345	12	1.1	2.86	1.88	1.15
277 Elvira	9/23/2017	bd-04 5927	10:35	2040	136	12:45	450	20	0.5	2.62	1.62	1.54
352 Gisela	2/25/2020	PPM 156693	10:58	1680	112	12:15	150	10	0.65	2.34	1.36	2.57
364 Isara	10/12/2017	HD 12356	11:50	1320	88	10:35	360	8	0.45	1.94	0.95	7.63
462 Eriphyla	10/30/2017	HD 13303	9:49	1830	122	7:40	360	12	0.44	2.67	1.68	1.81
703 Noemi (2019-09-25)	9/25/2019	HD 224448	10:00	4320	144	14:18	300	10	0.48, improving to 0.3	2.30	3.29	0.59
808 Merxia (2017-03-03)	3/3/2017	HD 97441	10:15	1590	122	7:56	300	12	0.91	2.59	1.61	2.59
913 Otila	5/19/2020	HD 138186	9:57	2880	192	13:11	300	12	0.195	1.91	0.91	4.55

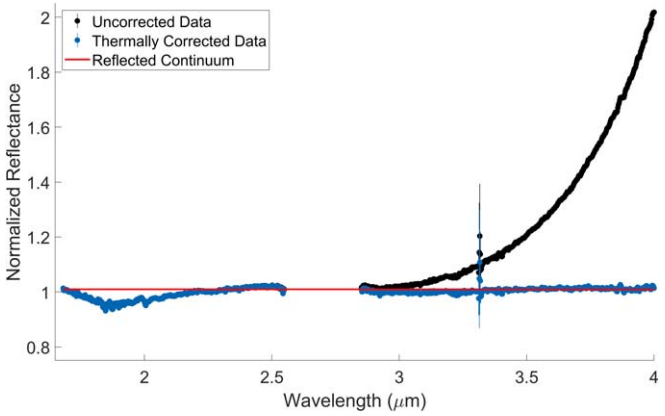

Figure 1. Example of an uncorrected LXD spectrum, reflected continuum, and thermally corrected data.

quantity with the following equation:

$$T_{\rm eq} = \left[\frac{(1 - A_{\rm B})F_{\rm Sun}}{(0.756 \cdot \varepsilon \cdot \sigma) \cdot r_H^2}\right]^{\frac{1}{4}}.$$

$F_{\rm Sun}$ is the flux of the Sun at 1 au (1365 W m^{-2}), ε is the infrared emissivity set to a value of 0.9, and σ is the Stephan–Boltzmann constant (5.67×10^{-8} W m^{-2} K^{-4}). The parameter r_H is the instantaneous heliocentric distance for each object at the time of observation. $A_{\rm B}$ is the Bond albedo. For asteroids, we use the treatment of Bowell et al. (1978) to calculate this quantity:

$$A_{\rm B} = pv \cdot (0.290 + 0.684 \cdot G),$$

where pv is the geometric albedo in the visible wavelengths and G is the magnitude slope (both values are taken from Horizons[4] for each asteroid).

The thermal model parameters and the equilibrium temperature for each asteroid are listed in Table 2. Thermally corrected data appear in Section 4.2.

2.4. Asteroids Physical and Orbital Characteristics

We gathered a number of physical and orbital parameters for each asteroid observed in this work. These include absolute magnitude, albedo, diameter, rotation period, semimajor axis, perihelion and aphelion distances, and spectral taxonomic type (s). All of these parameters were gathered from the JPL Horizons database. In addition to the orbital and physical parameters, we also used the asteroid spectrum classification tool[5] to produce principal component analysis of our near-infrared spectra. This web tool uses the Bus–DeMeo taxonomy framework (F. E. DeMeo et al. 2009), and the tool itself was developed at MIT by Stephen Slivan. We are primarily concerned with the slope of the spectrum. The other principal components are included in Appendix A. All of the quantities used in the subsequent sections can be found in Table 3.

3. Previous Observations of Asteroids in This Study

The majority of the asteroids in this study have taxonomic classifications but do not have reported interpretations of their near-infrared or 3 μm spectroscopy, including (5) Astrea, (30) Urania, (33) Polyhymnia, (39) Laetita, (67) Asia, (103) Hera, (115) Thyra, (151) Abunditia, (182) Elsa, (208) Lacrimosa, (277) Elvira, (352) Gisela, (462) Eriphyla, (703) Noemi, and (913) Otila. Nine of the asteroids presented in this work have been previously studied using near-infrared spectroscopy (e.g., (3) Juno, J. Degewij et al. 1979; K. Shinokawa et al. 2002; J. W. Noonan et al. 2019; (6) Hebe, C. R. Chapman & J. W. Salisbury 1973, F. Migliorini et al. 1997; P. Broglia et al. 1994; (7) Iris, J. W. Noonan et al. 2019; P. Vernazza et al. 2010; (8) Flora, E. A. Cloutis et al. 1990; (9) Metis, F. Marchis et al. 2006; M. S. Kelley & M. J. Gaffey 2000; (11) Parthenope, P. Vernazza et al. 2010; (808) Merxia and (17) Thetis, J. M. Sunshine et al. 2004; (364) Isara, P. Vernazza et al. 2010). M. J. Gaffey et al. (1993) also reported the near-infrared spectra of a large number of the objects observed in this work. All previous analyses are consistent with a nominally anhydrous composition.

For the purposes of this paper, we are primarily interested in the asteroid's potential hydration state. Only two asteroids (Hebe and Flora) have been previously observed with 3 μm spectroscopy. A. S. Rivkin et al. (2001) report observations of (6) Hebe. Rivkin and coauthors suggested that there are variations across Hebe's surface in 3 μm band depth and that Hebe may be an aqueously altered body. Observations of (8) Flora presented in N. Eaton et al. (1983) do not indicate evidence of hydration.

4. Results

4.1. Near-infrared Spectra

Presented in Figure 2 are the near-infrared spectra for each object in this study. All of the asteroids classify in the S-complex. The prism mode of the IRTF+SpeX instrument covers the wavelength range from ~0.7 to 2.5 μm. Further discussion of the near-infrared data, including derivation and interpretation of mineralogy, can be found in Appendix A.

Using the results from the band parameter analysis described in Appendix A, we assess the mineralogy of our sample. We impose minimum errors of 0.01 for band center and 0.1 for band area ratio (BAR) to account for systematic errors in the data, consistent with C. A. Thomas et al. (2014) and references therein. In Figure 3, we present the "Gaffey plot" of Band I center versus BAR. We overplot our data with the S-type subclasses presented in M. J. Gaffey et al. (1993).

The S-complex asteroids observed in this work exhibit a wide range of mineralogies from olivine dominated to basaltic achondrite mineralogy. The majority (17/33) of the observations are consistent with the S(IV) subclass, which is also referred to as the "ordinary chondrite boot." Asteroids in this particular field are consistent with ordinary chondrites (M. J. Gaffey et al. 1993) and potentially partially differentiated primitive achondrites (e.g., M. P. Lucas et al. 2019).

Descriptions of the mineralogy inferred from the band parameter analysis of the near-infrared spectra for all the asteroids in this study are presented in Table 4.

4.2. 3 μm Spectroscopy of Sample

The thermally corrected LXD spectra of the asteroids in this sample are presented in Figure 4. The LXD spectra of the S-type asteroids observed in this work show an absorption band with a flat shape between 2.9 and 3.4 μm. Middle and outer

[4] https://ssd.jpl.nasa.gov/horizons/
[5] http://smass.mit.edu/cgi-bin/busdemeoclass-cgi

Table 2
Thermal Model Parameters

Object	V Band/K Band[a]	Beaming Parameter	Reflectance at 2.45 μm	Continuum Slope (μm $^{-1}$)	T (K)
3 Juno	⋯	⋯	⋯	⋯	299.17
5 Astrea	1.11	0.7	1.02	⋯	296.91
6 Hebe	1.235	0.8	1.025	0.04	280.18
7 Iris (2018-12-13)	1.235	0.9	1.1	⋯	248.34
8 Flora	1	0.9	1.005	0.025	284.83
9 Metis	1.35	0.8	1.035	⋯	286.05
11 Parthenope	1.22	1	1.035	0.05	254.92
14 Irene (2019-10-03)	1.17	0.7	1.025	0.035	236.21
14 Irene (2020-02-03)	1.21	0.7	1.06	0.04	255.92
Irene (2017-02-15)	1.275	0.7	1.025	⋯	292.48
17 Thetis (2018-12-16)	1.5	1.2	1.06	⋯	225.96
17 Thetis (2019-05-15)	1.11	0.8	1.02	0.04	271.54
18 Melpomene	1.76	0.9	1.07	⋯	299.01
20 Massalia	1.235	0.9	1	⋯	279.97
30 Urania	1.375	0.9	1.06	0.15	279.75
33 Polyhymnia	1.25	1.1	1.1	⋯	270.48
39 Laetitia	1.257	0.75	1.05	0.08	266.18
63 Ausonia	1.4375	0.9	1.03	0.1	272.61
67 Asia	1.17	0.7	1.055	0.025	263.83
82 Alkmene	1.02	0.75	1.025	⋯	289.48
103 Hera (2020-09-20)	1.29	0.9	1	⋯	249.35
115 Thyra	1.17	0.8	1.01	0.02	260.81
151 Abunditia	1.54	1.2	1.03	0.01	273.9
182 Elsa (2019-10-03)	1.33	0.9	1.05	⋯	305.42
182 Elsa (2020-09-26)	1.15	0.7	1.03	0.055	280.77
208 Lacrimosa	1.33	0.7	1.1	⋯	255.81
277 Elvira	1.235	0.7	1.05	0.05	267.49
352 Gisela	1.5	0.9	1.035	⋯	273.77
364 Isara	1.54	0.9	1.07	⋯	308.03
462 Eriphyla	1.29	1.6	1.2	0.05	214.25
703 Noemi (2019-09-25)	1.33	0.7	1.12	⋯	282.71
808 Merxia (2017-03-03)	1.125	0.9	1.17	0.03	252.21
913 Otila	1.16	1	1.1	0.05	337.75
115 Thyra (PRISM only)	na	Na	na	na	na

Note.
[a] V band/K band is the ratio of reflectance at 0.55 μm to the reflectance at 2.2 μm.

main belt asteroids with significant hydration typically exhibit either checkmark-like features or bowl-like features. The S-complex asteroids are spectrally distinct from low-albedo objects. Similarly, they are generally distinct from nominally anhydrous near-Earth asteroids also observed in the 3 μm region (L. E. McGraw et al. 2022). McGraw et al. presented spectra of S- and Q-type near-Earth asteroids showing a variety of band shapes. This is discussed further in Section 5.2.

Table 3
Physical and Orbital Properties

Object	H[a]	G	Albedo	D (km)	Rotation Period [b] (hr)	SMASS II	Tholen
3 Juno	5.3	0.32	0.21[c]	246.6[a,c]	7.21	Sk	S
5 Astrea	6.9	0.15	0.27[a,c]	106.7[a,c]	16.81	S	S
6 Hebe	5.8	0.24	0.24[d]	185.2[d]	7.27	S	S
7 Iris (2018-12-13)	5.6	0.15	0.28[d]	199.8[d]	7.14	S	S
8 Flora	6.5	0.28	0.23[a,c]	147.5[a,c]	12.87	⋯	S
9 Metis	6.3	0.17	0.12[e]	190[f]	5.08	⋯	S
11 Parthenope	6.5	0.15	0.19[a,c]	142.9[a,c]	13.72	Sk	S
14 Irene (2019-10-03)	6.5	0.15	0.16[e]	152[f]	15.03	S	S
14 Irene (2020-02-03)	6.5	0.15	0.16	152	15.03	S	S
Irene (2017-02-15)	6.5	0.15	0.16	152	15.03	S	S
17 Thetis (2018-12-16)	7.7	0.15	0.19[a,c]	84.9[a,c]	12.27	Sl	S
17 Thetis (2019-05-15)	7.7	0.15	0.19	84.9	12.27	Sl	S
18 Melpomene	6.6	0.25	0.18[a,c]	139.6[a,c]	11.57	S	S
20 Massalia	6.5	0.25	0.24[a,c]	135.7[a,c]	8.1	S	S
30 Urania	7.5	0.15	0.19[a,c]	92.8[a,c]	13.69	Sl	S
33 Polyhymnia	8.5	0.33	0.24[a,c]	52.9[a,c]	18.61	Sq	S
39 Laetitia	6.1	0.15	0.27[a,c]	179.5[a,c]	5.15	S	S
63 Ausonia	7.4	0.25	0.13[a,c]	116[a,c]	9.30	Sa	S
67 Asia	8.3	0.15	0.1[a,c]	56.3[a,c]	15.85	S	S
82 Alkmene	8.2	0.28	0.17[a,c]	57.6[a,c]	12.99	Sq	S
103 Hera (2020-09-20)	7.6	0.15	0.22[a,c]	83.9[a,c]	23.74	S	S
115 Thyra	7.6	0.12	0.27[d]	79.8[d]	7.21	S	S
151 Abunditia	9.2	0.15	0.19[a,c]	39[a,c]	9.86	Sl	S
182 Elsa (2019-10-03)	9.1	0.15	0.20[a,c]	39.5[a,c]	80.09	S	S
182 Elsa (2020-09-26)	9.1	0.15	0.20	39.5	80.09	S	S
208 Lacrimosa	9.2	0.15	0.21[a,c]	40.1[a,c]	14.09	Sk	S
277 Elvira	9.9	0.15	0.20[a,c]	30.4[a,c]	29.69	⋯	S
352 Gisela	10.1	0.15	0.20[a,c]	26.7[a,c]	7.49	Sl	S
364 Isara	9.9	0.15	0.30[a,c]	25.9[a,c]	9.16	⋯	S
462 Eriphyla	9.4	0.15	0.26[a,c]	34.3[a,c]	8.66	S	S
703 Noemi (2019-09-25)	12.5	0.15	0.37[a,c]	7.3[a,c]	200	⋯	⋯
808 Merxia (2017-03-03)	9.8	0.15	0.21[a,c]	30.9[a,c]	30.63	⋯	L or S
913 Otila	12	0.15	0.28[a,c]	11.6[a,c]	4.87	⋯	S or Sq

Object	a (au)	e (deg)	i (deg)	Perihelion Distance (au)	Aphelion Distance (au)	Period (yr)
3 Juno	2.67	0.257	12.99	1.98	3.35	4.36
5 Astrea	2.57	0.191	5.37	2.08	3.07	4.13
6 Hebe	2.43	0.203	14.74	1.93	2.92	3.78
7 Iris (2018-12-13)	2.39	0.230	5.52	1.84	2.94	3.69

Table 3
(Continued)

Object	a (au)	e (deg)	i (deg)	Perihelion Distance (au)	Aphelion Distance (au)	Period (yr)
8 Flora	2.20	0.156	5.89	1.86	2.54	3.27
9 Metis	2.39	0.123	5.58	2.09	2.68	3.69
11 Parthenope	2.45	0.100	4.63	2.21	2.70	3.84
14 Irene (2019-10-03)	2.59	0.166	9.12	2.16	3.02	4.16
14 Irene (2020-02-03)	2.59	0.166	9.12	2.16	3.02	4.16
14 Irene (2017-02-15)	2.59	0.166	9.12	2.16	3.02	4.16
17 Thetis (2018-12-16)	2.47	0.133	5.59	2.14	2.80	3.88
17 Thetis (2019-05-15)	2.47	0.133	5.59	2.14	2.80	3.88
18 Melpomene	2.30	0.218	10.13	1.80	2.80	3.48
20 Massalia	2.41	0.143	0.71	2.07	2.75	3.74
30 Urania	2.37	0.128	2.10	2.06	2.67	3.64
33 Polyhymnia	2.87	0.332	1.85	1.92	3.83	4.87
39 Laetitia	2.77	0.112	10.37	2.46	3.08	4.61
63 Ausonia	2.40	0.127	5.78	2.09	2.70	3.71
67 Asia	2.42	0.185	6.03	1.97	2.87	3.77
82 Alkmene	2.76	0.220	2.83	2.15	3.37	4.59
103 Hera (2020-09-20)	2.70	0.079	5.42	2.49	2.92	4.44
115 Thyra	2.38	0.193	11.59	1.92	2.84	3.67
151 Abunditia	2.59	0.034	6.43	2.51	2.68	4.18
182 Elsa (2019-10-03)	2.42	0.187	2.01	1.97	2.87	3.76
182 Elsa (2020-09-26)	2.42	0.187	2.01	1.97	2.87	3.76
208 Lacrimosa	2.89	0.012	1.75	2.86	2.93	4.92
277 Elvira	2.88	0.092	1.16	2.62	3.15	4.90
352 Gisela	2.19	0.150	3.38	1.87	2.52	3.25
364 Isara	2.22	0.149	6.00	1.89	2.55	3.31
462 Eriphyla	2.87	0.088	3.19	2.62	3.13	4.87
703 Noemi	2.18	0.137	2.46	1.88	2.47	3.21
808 Merxia	2.75	0.129	4.72	2.39	3.10	4.55
913 Otila	2.20	0.171	5.81	1.82	2.57	3.26

Notes.
[a] H magnitudes are derived from IRAS observations, when reported.
[b] Rotation periods are from the Lightcurve Data Base (B. D. Warner et al. 2021)
[c] NEOWISE (J. R. Masiero et al. 2014).
[d] IRAS (E. F. Tedesco 2004).
[e] TRIAD (B. Zellner 1979).
[f] D. W. Dunham & D. Herald (2006).

4.2.1. 3 μm Band Depth Methodology

After thermally modeling each asteroid's LXD data (described in Section 2.3), the band depth for each object is determined. To do this, we take the mean of the data (rb) and the reflected continuum (rc) within $3.0 \pm 0.025\,\mu$m. The $3.0\,\mu$m band depth is defined as the difference between the averaged continuum values and the averaged data values divided by the averaged continuum values:

$$\text{band depth} = \frac{(\text{rc} - \text{rb})}{\text{rc}}.$$

Error is estimated as the standard deviation of the spectrum at $3.0 \pm 0.025\,\mu$m.

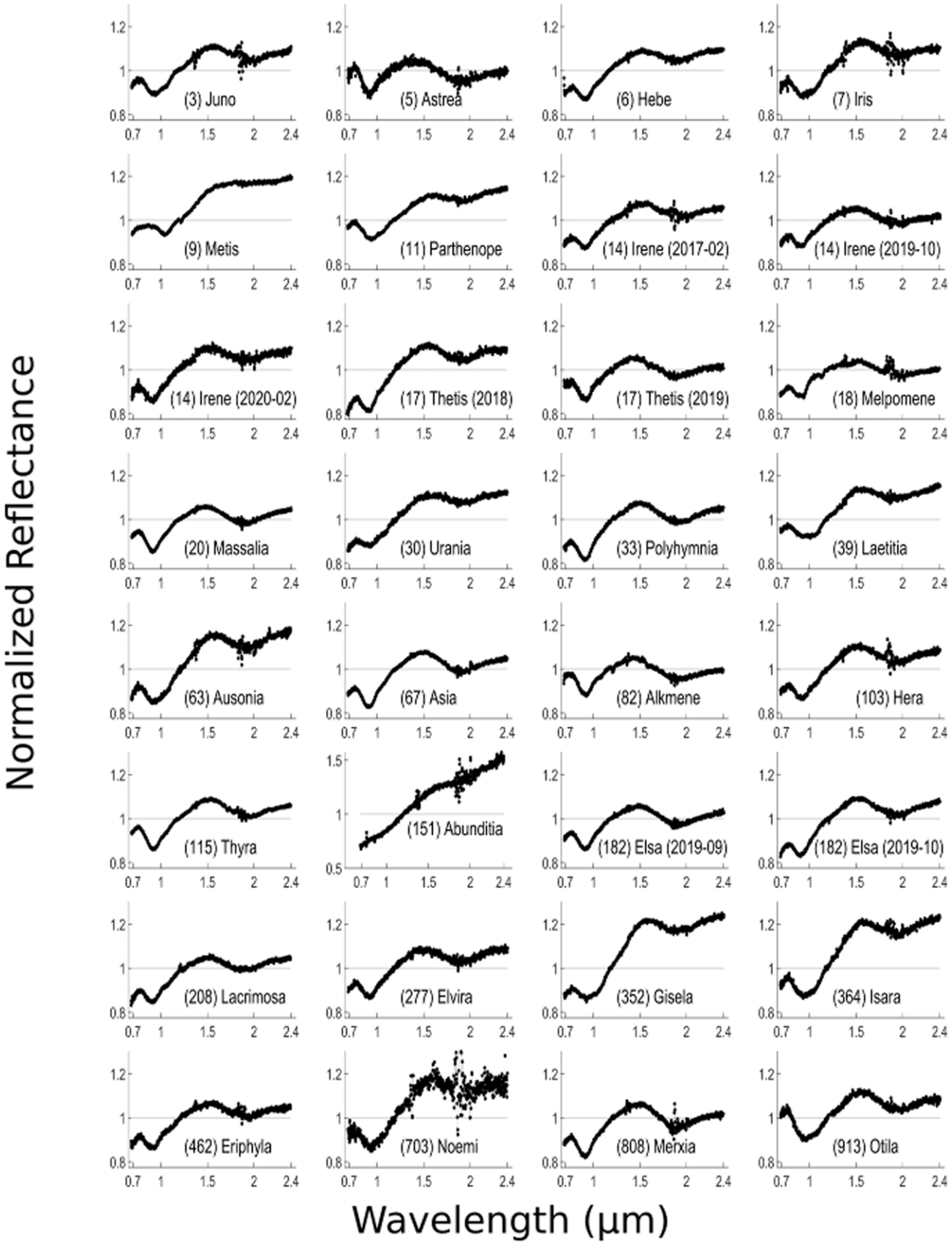

Figure 2. Near-infrared data of the observed asteroids.

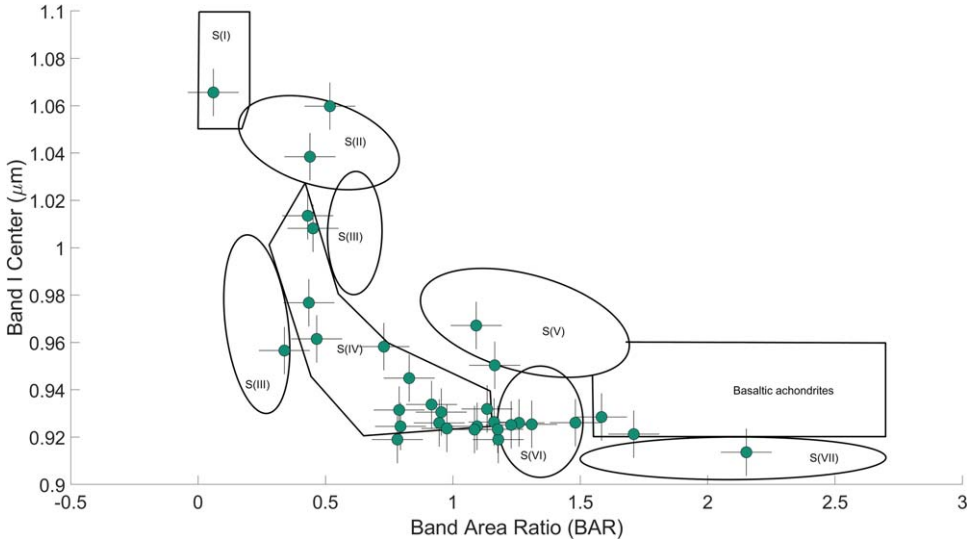

Figure 3. BAR vs. Band I center (Gaffey plot). Here we present the results of the band parameter analysis and S-type subclasses based on the M. J. Gaffey et al. (1993) plot. The nominally anhydrous asteroids we observed exhibit a wide variety of mineralogy from olivine dominated to basaltic achondrites. The majority of the objects are classified as S(IV) (ordinary chondrite boot) and S(VI) subtypes.

4.3. 3 μm Band Depths

4.3.1. 4 μm Band Depth Results

The 3 μm band depths for the objects in this study are presented in Table 5. For the 33 LXD observations of the 29 objects reported in this study, we find that all but six of the asteroids have a detectable 3.0 μm band of $\gtrapprox$1% depth within the error of the measurement. Band depths for the observed S-type asteroids range from $\sim$1.8% $\pm$ 0.11% to 12.5% $\pm$ 1.5%. This indicates the presence of OH/H_2O on the surfaces of 23 nominally anhydrous S-type asteroids within error. Given our current understanding of the presence of water on the surfaces of "dry" airless bodies like the Moon (R. N. Clark 2009; C. M. Pieters et al. 2009; J. M. Sunshine et al. 2009) and near-Earth objects (e.g., L. E. McGraw et al. 2022), this result may not be surprising; however, several of these objects have unexpectedly deep 3.0 μm bands.

Nine of the 29 objects have 3.0 μm band depths of $\gtrapprox$5%, with three asteroids having $\gtrapprox$10% band depths. Surprisingly, these deeper 3.0 μm band depths are consistent with the 3.0 μm band depths reported for hydrated low-albedo asteroids in the middle and outer main belt (Figure 5; D. Takir & J. P. Emery 2012).

4.3.2. OH/H_2O Band Depth Discussion

Hebe is known to have surface heterogeneity (e.g., C. R. Chapman & J. W. Salisbury 1973; P. Broglia et al. 1994; F. Migliorini et al. 1997). A. S. Rivkin et al. (2001) presented two 3 μm spectra of Hebe where they also saw differences in 3 μm band depth. The 3 μm spectrum presented here does not have a detectable band (e.g., $\sim$1.7% $\pm$ 1.8%). It seems that we observed the part of Hebe's surface with minimal hydration rather than the part of the surface with more significant hydration from A. S. Rivkin et al. (2001). Our spectrum is visually consistent with the "less hydrated" Hebe spectrum from A. S. Rivkin et al. (2001).

A. Arredondo et al. (2024) investigated four of the asteroids presented here using mid-infrared spectroscopy from the Stratospheric Observatory for Infrared Astronomy covering 4.9–13.7 μm ((7) Iris, (11) Parthenope, (18) Melpomene, and (20) Massalia). Arredondo et al. find that two asteroids, (7) Iris and (20) Massalia, have a 6 μm feature, which is an unambiguous detection of molecular water on their surfaces. (7) Iris and (20) Massalia have estimated water abundances of 374 $\pm$ 202 μg g^{-1} and 476 $\pm$ 219 μg g^{-1} of molecular water on their surfaces, respectively. Arredondo et al. note that this abundance of molecular water is consistent with values of molecular water detected on the sunlit surface of the Moon (e.g., C. I. Honniball et al. 2021, 2022).

C. I. Honniball et al. (2021) suggested that the molecular water detected on the sunlit lunar surface is likely created through micrometeorite impacts that have sufficient energy to create H_2O molecules. The molecular water on the lunar surface is likely trapped in impact glass, which prevents it from sublimating away. Impacts on the Moon generally have more kinetic energy compared to the average relative impact velocities in the asteroid belt. However, W. F. Bottke et al. (1994) show that there are a wide variety of impact velocities that can occur in the main asteroid belt, for a given object and its unique orbital parameters. Furthermore, the distribution of impact velocities tends to be non-Gaussian, for asteroids with high eccentricity and inclination, and has a significant tail of high-velocity impacts for many objects. W. F. Bottke et al. (1994) also show that asteroids with high inclination and eccentricity can have significantly higher average impact velocities. High inclinations and eccentricities tend to increase the relative encounter speed when asteroid impacts occur, though impacts are generally more infrequent for asteroids on highly inclined or eccentric orbits. While higher-velocity impacts in the main belt may be less frequent than impacts on the Moon, it is possible that molecular water detected on (7) Iris and (20) Massalia could be trapped in impact glasses as hypothesized for the Moon. This is particularly true for (7) Iris, which has a high eccentricity (0.23) and a relatively high inclination (5.°5). Higher-velocity impacts may explain the signature of water on (7) Iris, with a 3 μm band depth of 5.56 $\pm$ 0.97, and the detection may indicate that (7) Iris had at least one high-velocity impact that produced water molecules.

Several of the asteroids in this study have a high eccentricity (>0.2; (6) Hebe, (18) Melpomene, (82) Alkmene, and (7) Iris)

Table 4
Descriptions of Derived Mineralogy

Object	S-type Subclass	M. J. Gaffey et al. (1993)	Inferred Mineralogy[a]	Indicators
3 Juno	S(IV)	S(IV)	L or LL chondrite	Indicated by Fa versus olivine abundance and Fs versus olivine abundance
5 Astrea	S(IV)		H chondrite	Indicated by Fa versus olivine abundance and Fs versus olivine abundance
6 Hebe	S(IV)	S(IV)	H chondrite	Indicated by Fa versus olivine abundance and Fs versus olivine abundance
7 Iris (2018-12-13)	S(IV)	S(IV)	LL chondrite	Indicated by Fa versus olivine abundance and Fs versus olivine abundance
8 Flora	n.a.			
9 Metis	S(I)	ungrouped	Olivine dominated	Strong Band I and weak Band II connoting minimal pyroxene
11 Parthenope	S(III)	S(IV)	clinopyroxene bearing	greater pyroxene abundance compared to ordinary chondrite lithology
14 Irene (2019-10-03)	S(I)		Olivine dominated	Strong Band I and weak Band II connoting minimal pyroxene
14 Irene (2020-02-03)	S(IV)		H chondrite	Indicated by Fa versus olivine abundance and Fs versus olivine abundance
Irene (2017-02-15)	S(VI)		Nonordinary chondrite	More olivine-poor than ordinary chondrites; less calcic pyroxene than S(V) asteroids
17 Thetis (2018-12-16)	S(IV)		H chondrite	Indicated by Fa versus olivine abundance and Fs versus olivine abundance
17 Thetis (2019-03-15)	S(IV)		Potentially primitive achondrite in the acapulcoite −lodranite clan	Indicated by BI and BII centers (M. P. Lucas et al. 2019)
18 Melpomene	S(VII)	S(V)	Potentially either mesosiderite (metal + basaltic composition) or basaltic anorthositic composition	Distinct Band I and Band II but weaker than basaltic achondrites and Vesta-type asteroids/HEDs; potential mesosiderite analog, feldspar rich-basalt, or metal-bearing V-type lithology
20 Massalia	S(VI)	S(VI)	Pyroxene-dominated object (more olivine-poor than ordinary chondrites)	More olivine-poor than ordinary chondrites; less calcic than S(V) asteroids
30 Urania	S(IV)		L chondrite	Indicated by Fa versus olivine abundance and Fs versus olivine abundance
33 Polyhymnia	S(VI)	S(IV)	Pyroxene-dominated object (more olivine-poor than ordinary chondrites)	More olivine-poor than ordinary chondrites; less calcic than S(V) asteroids
39 Laetitia	S(II)		Ureilite composition	Olivine and clinopyroxene with greater abundance of olivine
63 Ausonia	S(V)	S(III)	Calcic pyroxene and olivine	Above olivine/pyrxene mixing line
67 Asia	S(IV)	S(IV)	H-chondrite-like	Indicated by Fa versus olivine abundance and Fs versus olivine abundance
82 Alkmene	S(IV)	S(VI)	H-chondrite-like	Indicated by Fa versus olivine abundance and Fs versus olivine abundance
103 Hera (2020-09-20)	S(IV)		H- or L-chondrite-like	Fa versus olivine abundance indicates an L-type lithology, while Fs versus olivine abundance indicates either H or L type
115 Thyra (LXD)	n.a.	S(III)	n.a.	n.a.
115 Thyra (prism)	S(IV)	S(III)	H- or L-chondrite-like	Fa versus olivine abundance indicates H chondrite lithology, while Fs versus olivine abundances indicates either H or L chondrite
151 Abunditia	S(V)		Calcic pyroxene and olivine	Above olivine/pyrxene mixing line; equal abundances of both minerals

Table 4
(Continued)

Object	S-type Subclass	M. J. Gaffey et al. (1993)	Inferred Mineralogy[a]	Indicators
182 Elsa (2019-10-03)	Basaltic achondrite			Basaltic achondrite
182 Elsa (2020-09-26)	S(VI)		Pyroxene-dominated object (more olivine-poor than ordinary chondrites)	More olivine-poor than ordinary chondrites; less calcic than S(V) asteroids
208 Lacrimosa	S(VI)		Pyroxene-dominated object (more olivine-poor than ordinary chondrites)	More olivine-poor than ordinary chondrites; less calcic than S(V) asteroids
277 Elvira	S(IV)		Potentially primitive achondrite in the acapulcoite−lodranite clan	Indicated by BI and BII centers (M. P. Lucas et al. 2019)
352 Gisela	S(II)		Ureilite composition	Olivine and clinopyroxene with greater abundance of olivine
364 Isara	S(IV)	S(II)	LL-chondrite-like	Indicated by Fa versus olivine abundance and Fs versus olivine abundance
462 Eriphyla	S(IV)		H-chondrite-like	Indicated by Fa versus olivine abundance and Fs versus olivine abundance
703 Noemi (2019-09-25)	S(IV)		L- or LL-chondrite-like	Both Fa and Fs versus olivine abundance indicate either an L or LL chondrite lithology
808 Merxia (2017-03-03)	S(VI)		Pyroxene-dominated object (more olivine-poor than ordinary chondrites)	S(VI)
913 Otila	S(IV)		LL-chondrite-like	More olivine-poor than ordinary chondrites; less calcic pyroxene than S(V) asteroids

Note.
[a] See Appendices A and B for more details.

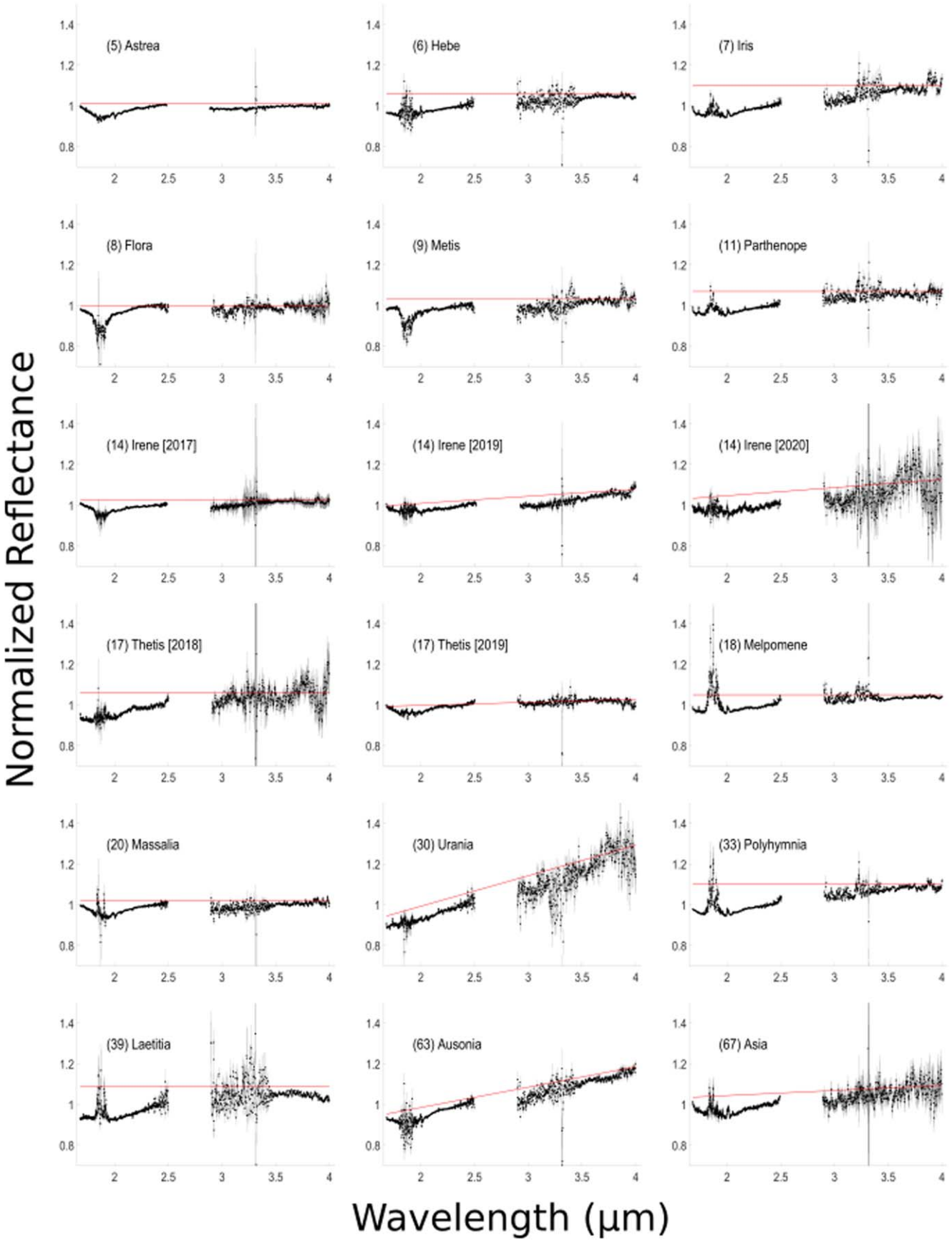

Figure 4. 3 μm observations of the asteroids in this study.

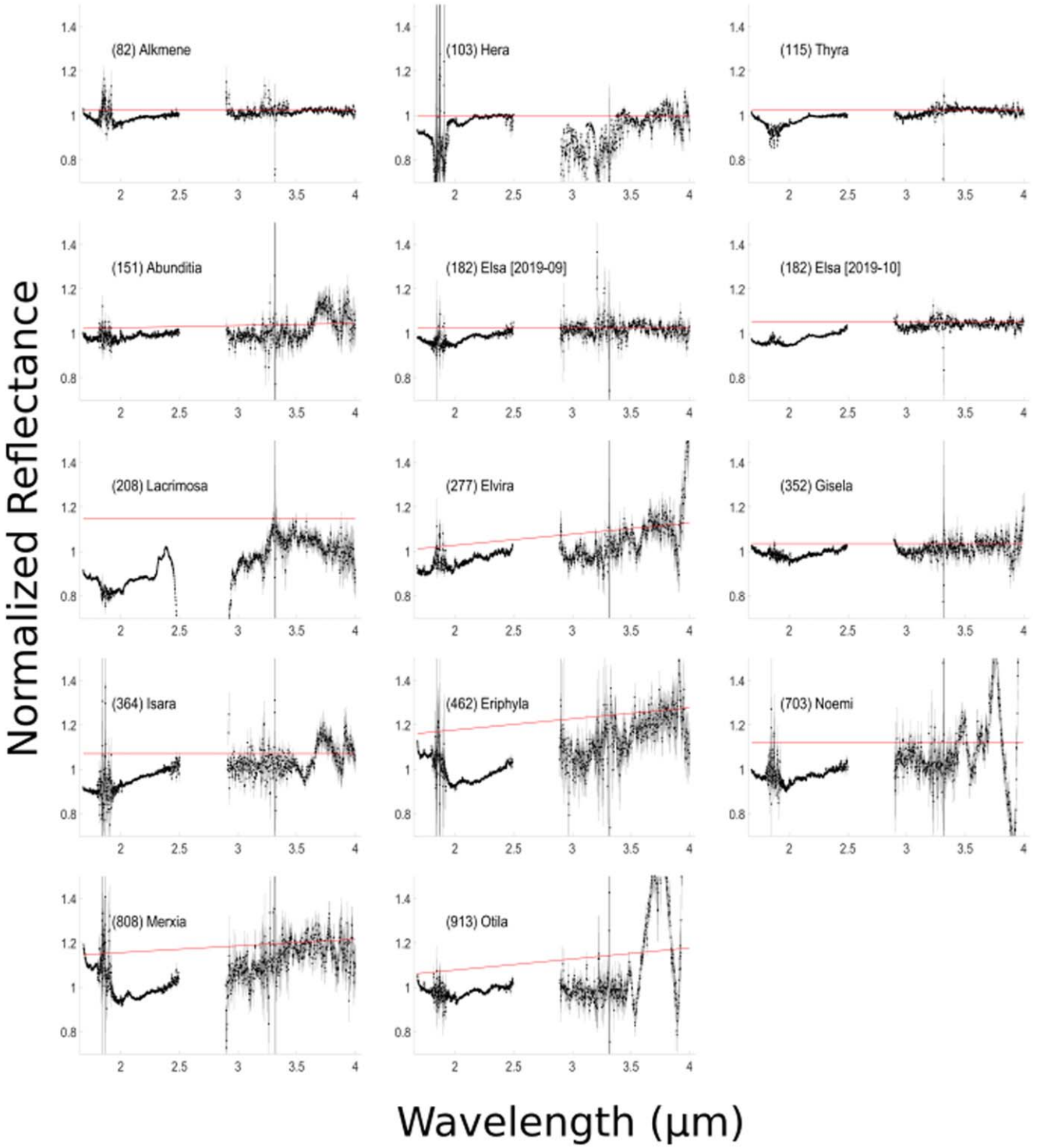

Figure 4. (Continued.)

and/or a high inclination (>10°; (18) Melpomene, (39) Laetitia, (115) Thyra, and (6) Hebe). (6) Hebe and (18) Melpomene have both a high eccentricity and a high inclination. (6) Hebe has a nondetection of a 3 μm absorption, indicating that it may not have experienced a sufficiently high velocity impact to produce water molecules through impacts as on the Moon or enough impacts to deliver exogenic materials. (18) Melpomene's detection of hydration may indicate the presence of water molecules. Further observations are required to investigate whether molecular water is present on its surface.

The nondetection of molecular water on (11) Parthenope by Arredondo et al. is not surprising given that our spectrum of Parthenope does not have a detectable 3 μm feature. Asteroid (7) Iris, on the other hand, has one of the deepest 3 μm bands in our survey (5.56% ± 0.97%). Given the A. Arredondo et al. (2024) results, some of the 3 μm signature observed here is

Table 5
3 μm Band Depth

Asteroid	3 μm Band Depth
3 Juno	n.a.
5 Astrea	1.87 ± 0.11
6 Hebe	1.73 ± 1.80
7 Iris (2018-12-13)	5.56 ± 0.97
8 Flora	1.26 ± 1.12
9 Metis	3.34 ± 1.5
11 Parthenope	1.02 ± 1.27
14 Irene (2019-10-03)	3.44 ± 0.25
14 Irene (2020-02-03)	5.21 ± 2.10
Irene (2017-02-15)	2.28 ± 0.64
17 Thetis (2018-12-16)	3.27 ± 1.81
17 Thetis (2019-05-15)	2.63 ± 0.6
18 Melpomene	3.02 ± 1.26
20 Massalia	3.02 ± 1.22
30 Urania	4.88 ± 2.92
33 Polyhymnia	3.78 ± 1.19
39 Laetitia	2.25 ± 4.05
63 Ausonia	3.28 ± 1.93
67 Asia	4.64 ± 1.45
82 Alkmene	2.45 ± 0.59
103 Hera (2020-09-20)	11.44 ± 4.6
115 Thyra	2.39 ± 0.56
151 Abunditia	4.53 ± 2.07
182 Elsa (2019-10-03)	1.99 ± 1.09
182 Elsa (2020-09-26)	2.34 ± 1.09
208 Lacrimosa	8.92 ± 2.85
277 Elvira	8.26 ± 1.37
352 Gisela	2.94 ± 1.09
364 Isara	2.78 ± 2.99
462 Eriphyla	10.36 ± 4.7
703 Noemi (2019-09-25)	3.32 ± 3.42
808 Merxia (2017-03-03)	5.29 ± 3.03
913 Otila	12.57 ± 1.52
115 Thyra (PRISM only)	n.a.

molecular water. However, not all of the 3 μm signatures for the S-complex asteroids presented in this work can be explained by molecular water. (18) Melpomene and (20) Massalia have very similar 3 μm bands, with depths of 3.0% ± 1.3% and 3.0% ± 1.0%, respectively. The fact that Melpomene has a nondetection of molecular water while (20) Massalia has molecular water indicates the complexity of the 3 μm bands for nominally anhydrous main belt S-type asteroids. There does not appear to be a single cause of the signature of hydration, but rather multiple factors are at play for the nominally anhydrous asteroids presented here. More 6 μm measurements of molecular water on nominally anhydrous asteroids are needed to further disentangle the contributions of water and OH to the 3 μm signatures on nominally anhydrous asteroids.

5. Implications

5.1. Mechanism(s) of Hydration: A Complex Interplay of Multiple Factors

To determine which mechanism is driving the signature of hydration on these nominally anhydrous objects, we look first at correlations between the 3 μm band depth and physical, orbital, and compositional characteristics, as well as observational circumstances. We investigated a wide variety of possibilities, which could point to a number of potential causes for the hydration state we see on these nominally anhydrous bodies.

Physical characteristics like size and albedo could indicate a relationship between hydration and asteroid formation processes, a size-dependent ability to retain volatiles, or subsequent geologic evolution of the asteroid. Any relationships with orbital characteristics might point to a dynamical component to the hydration state of S-complex asteroids. Additionally, some of the orbital characteristics, like semimajor axis and perihelion/aphelion distance, might also indicate a relationship between hydration state and proximity to hydrated asteroids, which are more populous in the middle and outer main belt or close to mean motion resonances. If any relationships exist here, we might consider the hydration effects to be related to exogenic material. We also wanted to consider the possibility that the hydration may be related to seasonality, which motivated the investigation of observational circumstances like instantaneous heliocentric distance and instantaneous theoretical equilibrium temperature. If the signature of hydration for our objects has a relationship with these parameters, it is possible that the hydration is caused by labile water/hydroxyl on the surfaces of these bodies similar to the diurnal cycle of lunar hydration (e.g., J. M. Sunshine et al. 2009). Finally, we included a few parameters in this analysis that might point to geometric effects and/or modeling effects that could call into question the validity of the reported 3 μm band depths.

All of the parameters we linearly regressed with respect to 3 μm band depth and the resulting relationships and statistics are given in Table 6. We include the coefficients of the regressions ($y = \mathrm{coef1}^{*}x + \mathrm{coef2}$), as well as the rms error (rmse), R, Student's t-value, P value, and R^2.

No physical, orbital, compositional, or circumstantial parameter seemed to have any strong or even moderate correlation with 3 μm band depth.

Here we consider the correlation coefficient, R, for the regressions. R values occur on a range of $[-1, 1]$, with negative values indicating a negative correlation and positive values indicating a positive correlation. Simply considering the magnitude of the correlations for R values, strong correlations would be $0.7 < |R| < 1$, moderate correlations would be $0.5 < |R| < 0.7$, weak correlations would be $0.3 < |R| < 0.5$, and negligible correlations would be $0.0 < |R| < 0.3$. We do not find any moderate or strong correlations between any parameter

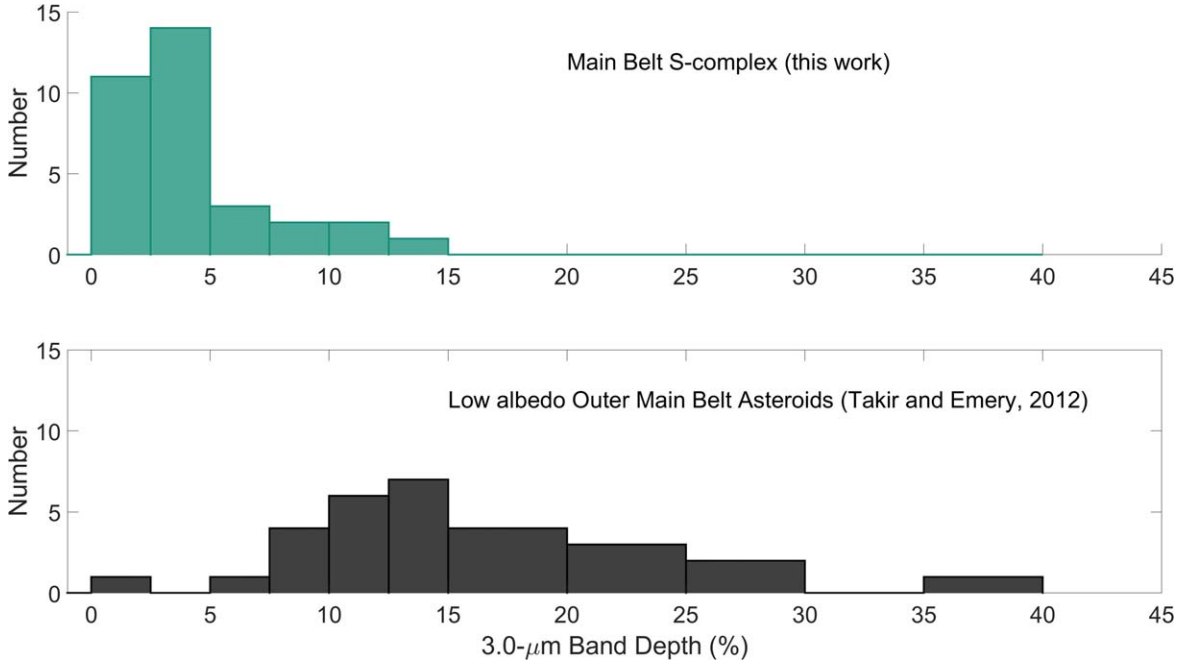

Figure 5. Histogram of 3 μm band depths for the nominally anhydrous S-complex asteroids (top) and values from low-albedo middle and outer main belt asteroids from D. Takir & J. P. Emery (2012) (bottom). Some of the S-complex asteroids studied in this work have 3 μm band depths that are consistent with hydrated asteroids.

considered and 3.0 μm band depth. Nominally anhydrous S-complex asteroids in the inner belt do not seem to be related to orbital characteristics, unlike low-albedo middle and outer main belt asteroids (e.g., D. Takir & J. P. Emery 2012). Multiple factors are likely at play.

Similarly, there is only a weak correlation with semimajor axis and a negligible correlation with near-infrared slope, which suggests that solar wind implantation may not be a primary driving factor of the 3 μm bands observed. Older (redder) surfaces are not more hydrated than younger ones, and those objects closer to the Sun (and therefore experiencing more flux of solar wind particles) are also not more hydrated. If solar wind implantation is affecting the 3 μm band on nominally anhydrous main belt asteroids, then this process is complex and not solely dependent on proximity to the Sun or strictly dependent on size. We hypothesized that orbital characteristics like the aphelion distance might have had some relationship with these nominally anhydrous objects' 3 μm signature. Of the weak correlations found, the parameter that seems to be best correlated with 3.0 μm band depth is perihelion distance (Figure 6).

Perihelion distance is correlated with 3.0 μm band depth ($R = 0.46$) such that with increasing perihelion distance 3.0 μm band depth also increases. Asteroids with greater perihelion distances spend more time farther out in the main asteroid belt. This might indicate that the signature of hydration could be related to proximity to hydrated asteroids in the middle and outer belt and thus that the signature of hydration is driven by exogenic delivery of carbonaceous material to these objects. This is similar to the L. E. McGraw et al. (2022) result where near-Earth asteroids are found to have a relationship between the signature of hydration and aphelion distance. L. E. McGraw et al. (2022) conclude that S-complex near-Earth asteroids may be hydrated owing to exogenic sources driven by proximity of the object's orbit to hydrated asteroids in the main belt. Though this correlation is weak, it seems to indicate that solar wind implantation is not a significant contributor to the signature of hydration on nominally anhydrous asteroids.

Still, the relationship between main belt nominally anhydrous asteroids and perihelion distance is a weak correlation, and it does not appear that a single factor controls the hydration we report. There is likely a complex interplay between multiple hydration mechanisms here (e.g., exogenic source(s) of hydrated material, target composition, primordially accreted water, dynamical evolution, and/or solar wind implantation).

5.2. Comparison to Near-Earth Asteroids

L. E. McGraw et al. (2022) report a large study of near-Earth asteroids using near-infrared and 3 μm spectroscopy. In this work they report the spectra of 29 near-Earth S- and Q-type asteroids with detections of hydration on eight objects. Additionally, they report 3 μm spectral shape groupings that include two varieties of bowls, as well as linearly increasing checkmark-like features. The multiple band shapes seem to indicate differences in origin of the 3 μm hydration signature (e.g., checkmark-like shapes more likely to be H implantation; wide bowls may be exogenous materials; narrow bowls may be either solar wind or a mix of exogenous materials and solar-wind-implanted H). Proximity to the low-albedo, hydrated middle and outer main asteroid belt seems to be a significant factor reported in the McGraw et al. work. Near-Earth objects that have large aphelion distances and therefore spend significant time in the asteroid belt seem to have 3 μm. Composition, additionally, seems to be a significant factor. Near-Earth asteroids with V-type taxonomic classification do not have detectable 3.0 μm bands.

Comparing the eight near-Earth asteroids that have a 3.0 μm feature, our main belt asteroid data set is broadly similar to the near-Earth asteroids. The near-Earth S- and Q-type asteroids tend to have band depths between 2.5% and 5%. Most of the main belt S-complex asteroids have similar band depths. It appears that our data set is mostly consistent with the results of

Table 6
Fit Statistics

Parameter	coef1	coef2	rmse	R	t	P	R^2	Comment
Perihelion distance	5.05	−6.49	2.38	0.46	2.84	0.008	0.212	Weak correlation
H magnitude	0.72	−1.53	3.81	0.42	2.57	0.0154	0.180	Weak correlation
Diameter	−0.019	5.97	105.07	−0.378	−2.23	0.0334	0.142	Weak correlation
Eccentricity	−17.78	6.94	4.25	−0.36	−2.13	0.0412	0.131	Weak correlation
Period	1.95	−3.49	0.56	0.34	2.00	0.055	0.118	Weak correlation
Semimajor axis	4.53	−7.10	1.91	0.33	1.94	0.061	0.112	Weak correlation
Cross-sectional area	−1.00E-04	5.17	13128	−0.32	−1.88	0.070	0.105	Weak correlation
eta	4.62	0.21	3.45	0.30	1.74	0.092	0.092	Weak correlation
Heliocentric distance	3.04	−2.92	1.98	0.29	1.68	0.102	0.086	Negligible correlation
Flux (1/semimajor axis^2)	−30.19	9.17	4.18	−0.28	−1.61	0.118	0.08	Negligible correlation
Inclination	−0.21	5.43	4.16	−0.24	−1.36	0.185	0.058	Negligible correlation
T_eq	−0.02	9.59	269.16	−0.16	−0.87	0.393	0.026	Negligible correlation
Phase	−0.07	4.69	6.15	−0.13	−0.74	0.464	0.018	Negligible correlation
delta	0.64	3.28	2.73	0.13	0.71	0.484	0.016	Negligible correlation
Albedo	6.12	2.95	4.05	0.12	0.65	0.519	0.014	Negligible correlation
BAR	−0.65	5.05	3.52	−0.1	−0.53	0.600	0.01	Negligible correlation
Rotation period (hr)	−0.007	4.43	41.01	−0.1	−0.54	0.592	0.01	Negligible correlation
Band II depth	−0.98	4.67	4.18	−0.08	−0.43	0.668	0.007	Negligible correlation
Aphelion distance	0.87	1.76	1.37	0.08	0.44	0.662	0.007	Negligible correlation
Band I center	−5.11	9.28	3.47	−0.07	−0.39	0.697	0.006	Negligible correlation
Band II center	−4.10	12.38	2.49	−0.07	−0.36	0.72	0.005	Negligible correlation
PCA slope	−1.47	4.59	4.30	−0.04	−0.22	0.827	0.002	Negligible correlation
Band I depth	−0.69	4.46	4.35	−0.01	−0.04	0.965	0.0001	Negligible correlation

L. E. McGraw et al. (2022) in that proximity to the more hydrated middle and outer belt seems to be one significant factor in a complex relationship with the signature of hydration. This, however, is where the similarities in our data sets end.

L. E. McGraw et al. (2022) report 3.0 μm band shape groupings (e.g., wide/narrow linear, wide/narrow bowls). The vast majority of the large main belt S-complex asteroids reported here have essentially flat spectra between 2.9 and 3.4 μm. This is to say that the reflectance between 2.9 and 3.4 μm is roughly the same reflectance value for all the large main belt S-complex asteroids presented here. There do not appear to be any shape groupings or variations in the 3 μm band shape, particularly for the large asteroids. We may see some similarities between (208) Lacrimosa and Type 1 (wide linear) checkmark shape, between (808) Merxia and Type 2 (narrow linear) checkmark shape, and between (277) Elvira, (352) Gisela, and (462) Eriphyla and Type 3 (wide bowl) shape. Yet 85% of the objects reported here are flat, and even those with some similarities may be caused by some lingering unameliorated telluric contamination. There may be a number of reasons for the lack of similarities between these two data sets.

The near-Earth asteroids reported in L. E. McGraw et al. (2022) are generally significantly smaller than the objects observed in the main belt. We report spectra for only two objects with diameters ∼10 km or less, whereas McGraw et al. present spectra for 18 objects of 10 km diameter or less (most of these are ∼5 km or less in size; we have no objects below 5 km diameter). We report spectra for six asteroids between 10 and 40 km in diameter. This difference in our samples is driven by the underlying characteristics of the two populations. The near-Earth asteroid population tends to be small, smaller than ∼40 km in size, while the main belt has a power-law distribution of asteroids of 1000 km or less. This difference in sizes and the greater distance to the asteroid belt result in an observational bias between the asteroid population investigated in this work and that of L. E. McGraw et al. (2022). Beyond their orbital characteristics, the asteroids reported in this work are typically at least one order of magnitude larger than the objects reported in L. E. McGraw et al. (2022).

It is intriguing that some of the main belt asteroids in this work with <40 km diameter do seem to have some spectral type similarity with McGraw et al. Type 3 band morphology. The near-Earth asteroid (1036) Ganymed has a diameter of ∼40 km also and exhibits Type 3 spectral characteristics. Based

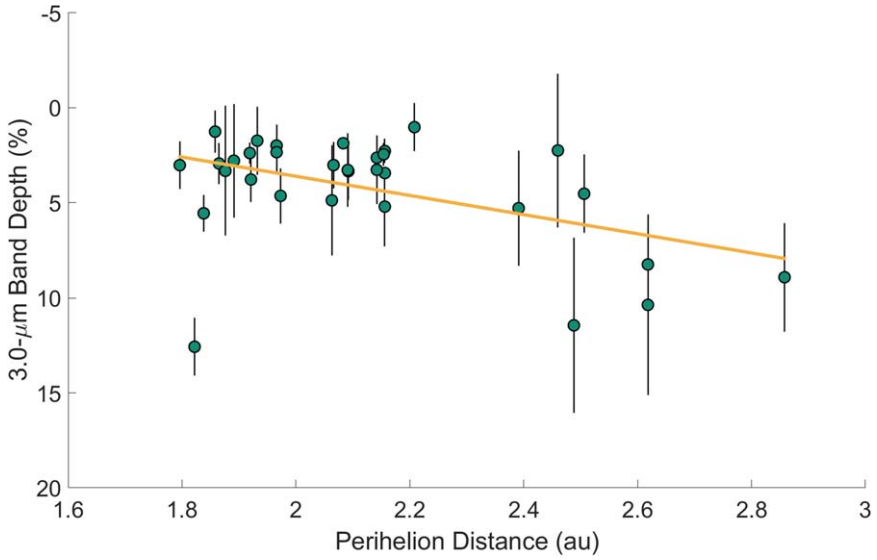

Figure 6. Perihelion distance vs. 3.0 μm band depth for all asteroids observed in this work. The relationship between perihelion distance and 3.0 μm band depth for the nominally anhydrous asteroids is weak, but it is the best correlation of all parameters that were considered. It seems that there are multiple factors driving the signature of hydration for nominally anhydrous objects. This correlation with perihelion distance could indicate that proximity to hydrated asteroids and exogenic material is one important factor among several hydration mechanisms.

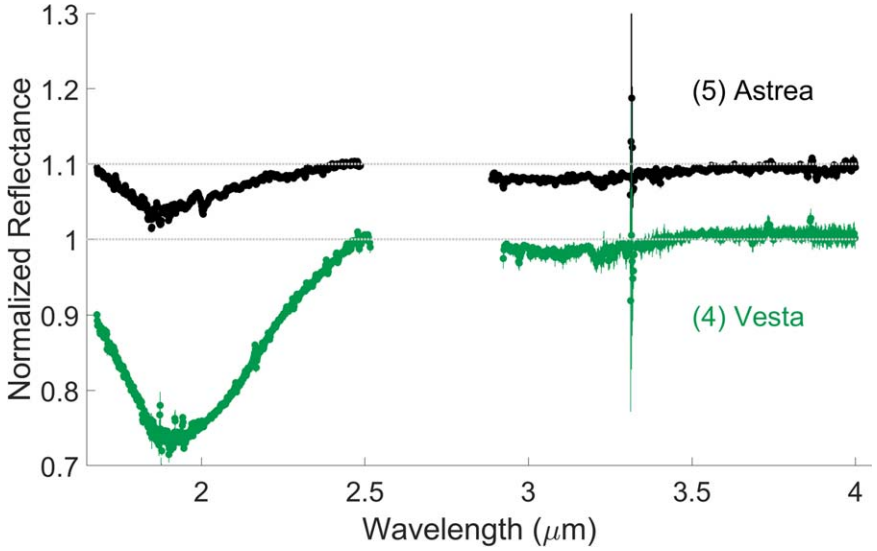

Figure 7. Comparison of an example S-complex asteroid ((5) Astrea) and (4) Vesta. Vesta was observed by IRTF, and this spectrum was published in L. E. McGraw et al. (2022). Vesta has a similar 3 μm band to the majority of the S-complex asteroids presented in this work. Vesta has a much deeper 2 μm band owing to Vesta's differentiated mineralogy. The leading explanation for the signature of hydration on Vesta is exogenic material. The similarity between Vesta and the S-complex asteroids supports the hypothesis that the 3 μm bands on S-complex asteroids are driven by exogenic material.

on recent missions to small near-Earth objects (M. Yoshikawa et al. 2006; D. N. DellaGiustina et al. 2019; T.-M. Ho et al. 2021), asteroids with very small diameters have significantly more boulders and large-grained regoliths. Perhaps larger grains interact differently with the solar wind and/or retain OH/H_2O differently than larger asteroids with finer-grained regoliths. More observations of main belt asteroids between 10 and 40 km would be necessary to investigate this hypothesis. Additionally, laboratory studies of the effect of grain size on solar wind implantation of OH could also further our understanding of the systematic differences between large and small asteroids.

5.3. Comparison to Vesta

L. E. McGraw et al. (2022) report a 3.0 μm detection for (4) Vesta, which is consistent with previous observations made using ground-based telescopes (S. Hasegawa et al. 2003) and global detections from the Dawn mission (M. C. De Sanctis et al. 2012). Vesta's 3.0 μm band is reported to be $2.4\% \pm 0.9\%$, which is also consistent with many of the S-complex asteroids reported in this work. Figure 7 shows a comparison to an IRTF spectrum of Vesta from L. E. McGraw et al. (2022) and an S-type asteroid ((5) Astrea). The spectrum reported in L. E. McGraw et al. (2022) appears to have a flat shape, like the S-complex asteroids presented here. The

consistency across Vesta and the nominally anhydrous main belt S-complex asteroids seems to support the hypothesis of exogenic material as a significant, though not sole, factor in the signature of hydration for large main belt S-complex asteroids.

Vesta was known to have a signature of hydration prior to the arrival of the Dawn spacecraft in 2011 (e.g., S. Hasegawa et al. 2003), and this signature was detected all over the surface (e.g., A. S. Rivkin et al. 2006). The Dawn mission globally mapped Vesta, confirming this detection (e.g., M. C. De Sanctis et al. 2012). Researchers found that the 3 μm band was associated with dark material on Vesta's surface (e.g., T. B. McCord et al. 2012; V. Reddy et al. 2012).

The presence of dark materials on Vesta's surface varies spatially, with detections in crater rims, walls, and ejecta blankets, as well as some exposures in Vesta's midlatitude hills (e.g., T. B. McCord et al. 2012; V. Reddy et al. 2012). V. Reddy et al. (2012) show that one large crater in particular, Venenia, has a high concentration of dark material in its crater walls. While other materials on Vesta can be dark (e.g., impact melts/shock-darkened materials, pyroclastic deposits, fine-grained eucrites with quenched textures, opaque materials such as metal and tochilinite), the association of 3 μm signatures with the Vestan dark material indicated that the composition is most similar to aqueously altered carbonaceous meteorites. These carbonaceous materials are inconsistent with any potential endogenic source on Vesta, so it was concluded that they were delivered from exogenic sources. This conclusion was further supported by the presence of unshocked carbonaceous clasts in howardite–eucrite–diogenite (HED) meteorites (e.g., A. E. Rubin & W. F. Bottke 2009). Carbonaceous-like clasts, A. E. Rubin & W. F. Bottke (2009) report, are the most abundant foreign clasts in HEDs.

Vesta, as one of the most studied asteroids, is an important comparison point for the S-complex asteroids in this study. Given that there are several potential scenarios for the delivery of exogenic hydrated materials to Vesta, we now consider whether similar delivery scenarios are possible for S-complex asteroids. First, it should be noted that carbonaceous chondrite clasts are also the most abundant foreign clasts found in H ordinary chondrites (A. E. Rubin & W. F. Bottke 2009). Given the potential link between some S-complex asteroids and ordinary chondrites, this observation serves as an independent confirmation of exogenic material.

If exogenic material is delivered by impacts, as hypothesized for Vesta (e.g., T. B. McCord et al. 2012; V. Reddy et al. 2012), there are several key factors involved in the estimate of its delivery. Impact velocity and the probability of impacts are the first key factors. According to W. F. Bottke et al. (1994), the impact probability and the distribution of relative impact velocities are unique to each asteroid, depending on its size and orbital parameters. The distribution of relative impact velocities for asteroids in the main belt with relatively small inclination and eccentricity tends to be non-Gaussian. Impacts may occur at velocities higher or lower than the average impact velocity in the asteroid belt. In the case of Vesta, ~6% of impacts would have been slow enough to allow a 10–30 km sized object impact and retain a significant proportion of the projectile material (e.g., V. Reddy et al. 2012). Asteroids on more inclined or eccentric orbits tend to have higher relative impact velocities compared to the average impact velocity of the main belt. The impact probability for asteroids on these orbits is lower because they do not cross as many objects as coplanar orbits. However, these higher impact velocities may be sufficiently energetic to form molecular water, similar to the process for lunar molecular water production (e.g., C. I. Honniball et al. 2021).

In the event that impacts occur with the right speed and angle, the amount of the projectile mass retained by the asteroid is the next critical factor. The amount of the impactor body that is retained on an asteroid is dependent on the target body's size, the relative impact speed, and the impact angle. According to hydrodynamic simulations and impact scaling laws presented in V. Svetsov (2011), slower impact velocities allow more impactor mass to be retained. However, for a given impact speed, smaller asteroids retain less impactor mass and significant target mass is lost in comparison to impacts on larger objects. Still, even for objects with sizes of ~50–200 km diameter at moderate (5 km s^{-1}) impact speeds and low (1.25 km s^{-1}) impact speeds, the retained impactor mass can range from 35% to 75%. These scaling laws are supported by laboratory studies that find significant survival of impactor mass and minimal impactor melting (C. Avdellidou et al. 2016).

While the S-complex asteroids studied in this work are smaller than Vesta, it may be possible that these bodies experienced exogenic material delivering impacts with sufficient retention that this exogenic material would be detectable today. The peculiarities that affect impact probability, speed, and retention are unique to each object and complex. The complexity involving size and orbital parameters may explain why we do not see any correlations of 3 μm band depth with other parameters. A detailed investigation of the probabilities of each asteroid in the style of D. P. O'Brien et al. (2011), T. B. McCord et al. (2012), and V. Reddy et al. (2012) is beyond the scope of this work. However, those investigations would likely provide insights into the signature of hydration detected on the asteroids presented here.

5.4. Investigating the H-ordinary-chondrite-like Asteroids

One potential way to begin to understand how multiple factors may be affecting the signature of hydration is to consider asteroids that have a strong compositional similarity. In general, there are two ways to investigate asteroids with a strong compositional similarity: collisional families or asteroids with strongly similar spectral properties. We do not have a sufficient number of asteroids within families to investigate how 3 μm band depth may vary. Still, we acknowledge that this could be a fruitful investigation in the future. Aside from investigating families, there is another method for exploring asteroids with compositional similarity.

As described in Appendix A, we see that a large subset of this sample of asteroids is consistent with ordinary-chondrite-like mineralogy, plotting in the ordinary chondrite boot region of the Gaffey plot (Figure 3). Further analysis described in Appendix B identifies asteroids that are compositionally consistent with H ordinary chondrites.

The H-ordinary-chondrite-like asteroids (Table 7) are the most numerous subgroup of objects in our study, representing ~30% of the objects/observations reported here. Additionally, there is some evidence that the H and L ordinary chondrites may have come from the same asteroid (K. Keil et al. 1994). We include the single L-like asteroid in these analyses as well. We now consider only these asteroids to investigate correlations between the parameters described above and this subset.

Table 7
H-ordinary-chondrite-like Asteroids

Asteroid	Subtype[a]
5 Astrea	H-ordinary-chondrite-like
6 Hebe	H-ordinary-chondrite-like
14 Irene (2020)	H-ordinary-chondrite-like
17 Thetis (2018)	H-ordinary-chondrite-like
30 Urania	L-ordinary-chondrite-like
67 Asia	H-ordinary-chondrite-like
82 Alkmene	H-ordinary-chondrite-like
103 Hera	H- or L-ordinary-chondrite-like
115 Thyra	H- or L-ordinary-chondrite-like
462 Eriphyla	H-ordinary-chondrite-like

Note.
[a] Derivation of these subtypes is described in Appendix B.

We proceed with these correlations with an abundance of caution. This is a very small number of objects, and any relationships that are found must be absorbed with a grain of metaphorical salt. More observations of nominally anhydrous asteroids, especially compositionally linked asteroids, are needed to confirm any relationships we find here.

Considering only the compositionally linked ordinary-chondrite-like asteroids, we find three strong correlations with 3.0 μm band depth: eccentricity ($R = 0.88$, $P = 0.00071$), perihelion distance ($R = 0.88$, $P = 0.0076$), and Band II center ($R = 0.72$, $P = 0.019$).

The strong correlation between the H-chondrite-like asteroids and perihelion distance (Figure 8) could hint that hydration is related to exogenic material. Similar to the conclusions of L. E. McGraw et al. (2022), the asteroids that have greater perihelion distances spend more of their time closer to the lower-albedo and generally more hydrated middle and outer main asteroid belt. The proximity to those objects could increase the likelihood of impacts of hydrated material. One contributing factor to the signature of hydration on nominally anhydrous asteroids could be exogenic material.

The R values of the eccentricity (Figure 9) and perihelion distance (Figure 8) correlations are nearly identical. This similarity may be driven by this underlying bias in the objects we observed. One potential cause of this underlying bias is that the inner main belt experienced a late excitation event that shaped the eccentricity distribution (e.g., R. Malhorta & X. Wang 2017). The asteroids in our data set with the greatest perihelion distance have the lowest eccentricities.

Band II is caused by the abundance and composition of pyroxene in S-complex asteroids and ordinary chondrites. The Band II center position's correlation with 3 μm band depth covers a very small change in Band II position. Because these objects are compositionally linked, this band has virtually the same position for all the objects in this subset. The difference in position is $\sim$0.05 μm. This is well within the error of the measurement, and so this correlation is likely spurious.

The relationship between eccentricity and band depth is a strong negative correlation (Figure 9): the asteroids with the deepest 3 μm bands have the lowest eccentricities, while asteroids with the shallowest 3 μm bands have the highest eccentricities. W. F. Bottke et al. (1994) show that asteroids with high inclination and eccentricity tend to have higher relative impact speeds. Impacts are less likely to occur for asteroids with higher eccentricity and/or inclination. Moreover, these impacts would retain less impactor mass and erode more target mass when they do occur (e.g., V. Svetsov 2011). The correlation with eccentricity may indicate that asteroids with more circular, coplanar orbits are more likely to experience lower-speed impacts, thus allowing them to retain more exogenic material compared to those asteroids on more eccentric orbits.

6. Conclusions

We have presented a large 3 μm survey of nominally anhydrous S-complex asteroids in the main asteroid belt. Our primary result is that 23 of the 29 objects we observe show the signature of hydration through the telltale 3 μm absorption. The objects in the study have variable amounts of hydration from very little ($\sim$1% band depth) to significant (>10% band depth), which is comparable to some of the hydrated low-albedo main belt objects (D. Takir & J. P. Emery 2012), though the shapes of the 3 μm band differ from low-albedo asteroids and S- and Q-type near-Earth asteroids (L. E. McGraw et al. 2022). Overall, it appears that hydration of nominally anhydrous asteroids is controlled by multiple factors; there is no single, straightforward explanation for the signature of hydration detected on nominally anhydrous asteroids in the main belt. Potentially, the signature hydration could be related to the perihelion distance of the asteroid. This correlation, however, is weak. This weak correlation suggests that solar wind implantation is perhaps not a significant source, as band depth increases with increasing perihelion. It follows that exogenic delivery of hydrated material may, however, be a significant source. When we investigate asteroids that appear to be consistent with H ordinary chondrite lithologies, which likely share compositional characteristics and parent-body evolution, we find that eccentricity and perihelion distance are strongly correlated with 3 μm band depth. This could indicate an exogenic source for the signature of hydration.

It seems likely that exogenic material is a significant driving factor of the signature of hydration for nominally anhydrous asteroids given the weak correlation with perihelion distance for the whole sample and the strong correlation with eccentricity for the H-ordinary-chondrite-like asteroids. Asteroids with lower eccentricity are more likely to experience low-speed impacts, which would enable exogenic material to be retained. Asteroids on more eccentric orbits tend to experience higher speed though less frequent impacts (e.g., W. F. Bottke et al. 1994). Exogenic delivery is still only one contributing factor to the signature of hydration observed. More observations are necessary to untangle what is driving the 3 μm signature.

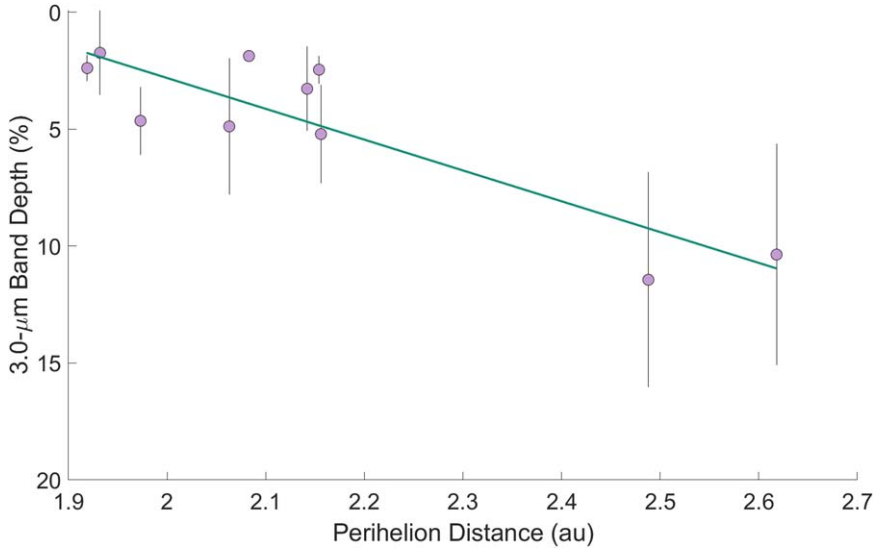

Figure 8. H-ordinary-chondrite-like asteroids' perihelion distance vs. 3.0 μm band depth. This (with eccentricity) is the strongest correlation for the H-ordinary-chondrite-like asteroids and their 3.0 μm band depth. This correlation indicates that the larger the perihelion distance, the deeper the 3.0 μm band. This may indicate that proximity to the lower-albedo, more hydrated middle and outer belt objects is a primary driver of the signature of hydration observed.

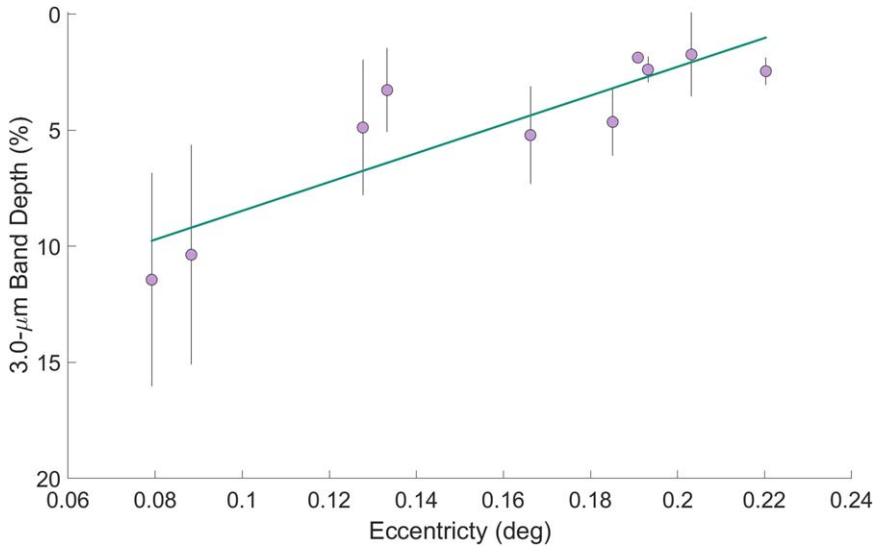

Figure 9. 3.0 μm band depth vs. eccentricity for H-ordinary-chondrite-like asteroids. For the objects in this study that are similar to H ordinary chondrites, eccentricity has the strongest relationship with 3.0 μm band depth. For asteroids with lower eccentricities, the band depth is deepest; for those with higher eccentricities, the band depth is shallower. Higher orbital eccentricities indicate dynamical excitation. Shallower band depths may indicate that the dynamical evolution is playing a part in band depths. Alternatively, asteroids with less dynamical excitation are more likely to be on nearly circular, coplanar orbits and may, therefore, likely have a greater flux of exogenic material compared to those with orbits that cause the asteroid to be out of the plane for much of its orbit.

Acknowledgments

This work was funded by Near-Earth Object Observations Program grant Nos. NNX16AE91G and 80NSSC20K0291

The data for this paper were collected at the Infrared Telescope Facility, which is operated by the University of Hawaii under contract 80HQTR19D0030 with the National Aeronautics and Space Administration.

Principle component analysis results presented in this work were determined, in whole or in part, using a Bus–DeMeo Taxonomy Classification web tool by Stephen M. Slivan, developed at MIT with the support of National Science Foundation grant 0506716 and NASA grant NAG5-12355.

Division of labor among coauthors: Observations: Thomas 17 runs (57%), McGraw 7.5 runs (25%), Emery 4.5 runs (15%), Richard Cartwright 1 run (3%). Data reduction: University of Tennessee (Knoxville) undergraduate supervised by McGraw and Emery 3 observations, McAdam 36 observations with significant support/troubleshooting from McGraw, Rivkin, Thomas, and Emery. Analysis: all performed by McAdam, with significant support from Thomas. Additional Data: reduced LXD observations of nominally anhydrous asteroids by Rivkin.

We thank Brittany Harvison and Juan Sanchez for cross-checking our band parameter analysis. We also thank Richard Cartwright for assisting in the data collection.

Appendix A
Mineralogy Inferred from Near-infrared Spectroscopy

To determine the relative abundances of minerals in the data set gathered, we begin by performing band parameter analyses to determine the centers and depths of the 1 and 2 μm bands, BAR, and associated errors with each measurement. The following methodology was used to calculate each element.

Prior to the band parameter analysis, we implemented a temperature correction for the 2 μm band. Temperature can affect near-infrared bands for asteroids with significant mafic materials on their surfaces (e.g., J. A. Sanchez et al. 2012 and references therein). These induced effects can cause the 2 μm band's position, width, and depth to shift. We use the methodology from J. A. Sanchez et al. (2012) to empirically correct the 2 μm band (Band II, or BII) using the following equation:

$$\Delta \mathrm{BII}\ (\mu\mathrm{m}) = 0.06 - 0.0002 \times T\,(\mathrm{K}).$$

A.1. Methodology

As stated above, the prism data for these S-complex asteroids typically have two distinct bands, one at 1 μm and the other at 2 μm. We call the 1 μm band "Band I" and the 2 μm band "Band II." To summarize, the band parameter analysis utilizes smoothed, continuum-removed spectral segments of the 1 and 2 μm bands to determine the band centers, depths, and areas of Band I and Band II. The BAR is defined as the quotient of Band II and Band I.

A.1.1. Spectral Segments

The band parameter analysis begins with defining the segments of each spectrum where Band I and Band II occur. The spectrum is passed to a function that smooths the data over a 0.036 μm window. The smoothing function returns an average value in a given window using a quadratic regression. Next, the endpoints of Band I and Band II are determined. Looking at an exemplary prism spectrum (Figure A1), there appear to be two local maxima around Band I. The first local maximum appears around 0.75 μm, and the other appears around 1.5 μm. The data within ~0.5 μm of each maxima are fitted with a cubic polynomial, and then the position of each maximum is determined by finding the peak of the polynomial function. The starting point of Band I is defined as the peak of the fitted polynomial around 0.75 μm. The end point of Band I is sometimes the peak of the fitted polynomial ~1.5 μm. However, Band I can sometimes terminate before this point.

For a number of asteroids in this sample we find that a continuum between the starting point of the Band I spectral segment and the local maximum ~1.5 μm sometimes crosses the data somewhere between 1.1 and 1.4 μm. This is defined as the "rollover" index because the data "roll over" the continuum. Using methodology consistent with C. A. Thomas et al. (2014), we define the Band I end point as the spot where the continuum drawn between the two local maxima around Band I intersects the spectrum itself.

Band II is determined by the position of the fitted polynomial for the local maxima ~1.5 μm and 2.4 μm. For all of the data in our study, we use the end point as 2.4 μm. Typically, the noise in the prism data gets very large at the end of the detector owing to edge effects, so we exclude everything longer that 2.4 μm to avoid the spuriously noisy data points.

Once the data have been smoothed and the Band I and Band II spectral segments have been defined, we perform a continuum removal of the data. The Band I and Band II continua are defined as straight lines between the endpoints of each segment. Band I and Band II spectral segments are then divided by the continuum, removing any effects of spectral slope from the underlying band parameters (right panel of Figure A1).

Using the methodology described in J. A. Sanchez et al. (2020), we determine Band I center. To briefly summarize, we select subsets of the Band I spectral segment with different starting and ending wavelengths and fit third and fourth-order polynomials to each portion of the smaller segment. We determine the position of the minima of each polynomial. The center position of Band I is defined as the mean of all the minima positions, and the error of this parameter is defined as the standard deviation of the minima positions.

The Band II center position is determined in a similar way to Band I. However, we utilize second- and third-order polynomials because this band is typically wider than Band I. The position and errors are the mean and standard deviation of the fitted minima, respectively, as for Band I.

Band I and Band II depths are calculated using a similar methodology described in C. A. Thomas et al. (2014). We take the difference between the continuum and the continuum-removed spectrum at the position of the band center. We define this as the band depth. To determine the error of this measurement, we modify the value of the spectrum at the band center position with the error of the spectrum at that point and a random number generated over the value of [−1, 1]. We repeat this process 20,000 times and then take a standard deviation of the synthetic band depths to estimate the error.

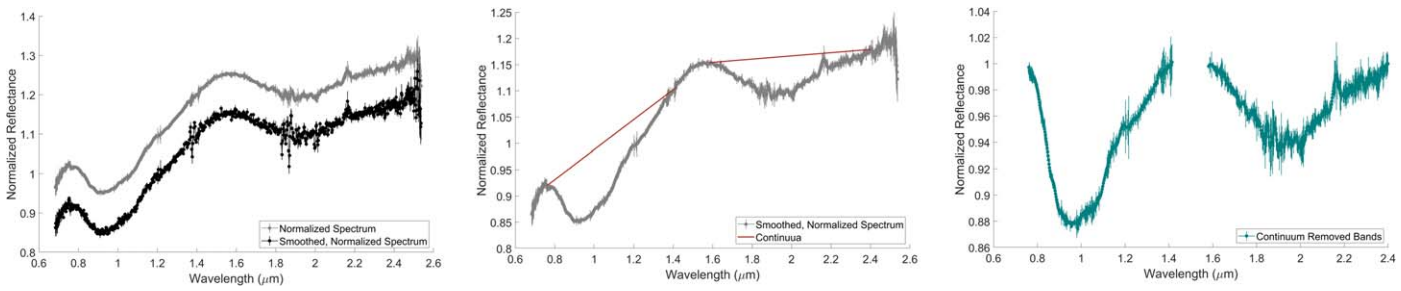

Figure A1. Defining spectral segments. Prism data (black) are first smoothed (left; gray spectrum offset by 0.1 for clarity), and then continua are defined as the local maximum ~0.75 μm and the "rollover" location or the local maximum near ~1.5 μm (middle). Finally, the continua are divided from the spectral segments and the band positions, depths, and areas are subsequently calculated (right).

Table A1
Band Parameter Analysis Results

Asteroid	BI Center (μm)	Band I Depth	Band II Center (μm)	Band II Depth	Band I Area	Band II Area	BAR
3 Juno	0.958 ± 0.01	0.066 ± 0.001	1.987 ± 0.014	0.184 ± 0.001	0.031 ± 0.707	0.023 ± 0.0707	0.729 ± 0.1
5 Astrea	0.925 ± 0.01	0.043 ± 0.001	1.914 ± 0.013	0.02 ± 0.004	0.029 ± 0.707	0.032 ± 0.0707	1.095 ± 0.1
6 Hebe	0.931 ± 0.01	0.036 ± 0.002	1.914 ± 0.051	0.208 ± 0.002	0.018 ± 0.707	0.018 ± 0.0707	0.954 ± 0.1
7 Iris (2018-12-13)	1.008 ± 0.01	0.104 ± 0.001	1.956 ± 0.044	0.222 ± 0.001	0.036 ± 0.707	0.018 ± 0.0707	0.451 ± 0.1
9 Metis	1.066 ± 0.01	0.086 ± 0.001	2.169 ± 0.028	1.173 ± 0.001	0.026 ± 0.707	0.002 ± 0.0707	0.06 ± 0.1
11 Parthenope	0.957 ± 0.01	0.066 ± 0.001	1.947 ± 0.046	0.208 ± 0.001	0.035 ± 0.707	0.013 ± 0.0707	0.339 ± 0.1
14 Irene (2019-10-03)	0.928 ± 0.01	0.001 ± 0.002	1.951 ± 0.031	1.003 ± 0.001	0.013 ± 0.707	0.022 ± 0.0707	1.583 ± 0.1
14 Irene (2020-02-03)	0.919 ± 0.01	0.05 ± 0.0001	1.942 ± 0.038	0.178 ± 0.0001	0.025 ± 0.707	0.02 ± 0.0707	0.782 ± 0.1
14 Irene (2017-02-15)	0.919 ± 0.01	0.05 ± 0.0001	1.935 ± 0.038	0.178 ± 0.0001	0.025 ± 0.707	0.02 ± 0.0707	1.178 ± 0.1
17 Thetis (2018-12-16)	0.926 ± 0.01	0.043 ± 0.002	1.916 ± 0.053	0.29 ± 0.001	0.021 ± 0.707	0.021 ± 0.0707	0.946 ± 0.1
17 Thetis (2019-05-15)	0.926 ± 0.01	0.047 ± 0.005	1.876 ± 0.039	0.106 ± 0.001	0.023 ± 0.707	0.028 ± 0.0707	1.162 ± 0.1
18 Melpomene	0.914 ± 0.01	0.021 ± 0.002	1.984 ± 0.01	0.056 ± 0.003	0.009 ± 0.707	0.019 ± 0.0707	2.152 ± 0.1
20 Massalia	0.923 ± 0.01	0.051 ± 0.003	1.909 ± 0.038	0.137 ± 0.002	0.026 ± 0.707	0.031 ± 0.0707	1.176 ± 0.1
30 Urania	0.945 ± 0.01	0.042 ± 0.001	1.942 ± 0.043	0.225 ± 0.001	0.015 ± 0.707	0.013 ± 0.0707	0.828 ± 0.1
33 Polyhymnia	0.926 ± 0.01	0.061 ± 0.001	1.921 ± 0.036	0.175 ± 0.002	0.024 ± 0.707	0.031 ± 0.0707	1.26 ± 0.1
39 Laetitia	1.06 ± 0.01	0.106 ± 0.001	1.968 ± 0.019	0.221 ± 0.001	0.034 ± 0.707	0.019 ± 0.0707	0.517 ± 0.1
63 Ausonia	0.967 ± 0.01	0.102 ± 0.001	1.944 ± 0.046	0.309 ± 0.003	0.042 ± 0.707	0.026 ± 0.0707	1.091 ± 0.1
67 Asia	0.923 ± 0.01	0.055 ± 0.002	1.912 ± 0.042	0.177 ± 0.001	0.026 ± 0.707	0.029 ± 0.0707	1.085 ± 0.1
82 Alkmene	0.924 ± 0.01	0.059 ± 0.001	1.901 ± 0.028	0.072 ± 0.001	0.027 ± 0.707	0.034 ± 0.0707	0.976 ± 0.1
103 Hera	0.934 ± 0.01	0.042 ± 0.002	1.954 ± 0.023	0.181 ± 0.002	0.024 ± 0.707	0.023 ± 0.0707	0.916 ± 0.1
115 Thyra (PRISM only)	0.925 ± 0.01	0.06 ± 0.001	1.939 ± 0.033	0.169 ± 0.002	0.033 ± 0.707	0.027 ± 0.0707	0.794 ± 0.1
151 Abunditia	0.95 ± 0.01	0.092 ± 0.003	1.951 ± 0.034	0.561 ± 0.003	0.008 ± 0.707	0.01 ± 0.0707	1.164 ± 0.1
182 Elsa (2019-10-03)	0.921 ± 0.01	0.041 ± 0.002	1.937 ± 0.031	0.196 ± 0.001	0.017 ± 0.707	0.029 ± 0.0707	1.71 ± 0.1
182 Elsa (2020-09-26)	0.926 ± 0.01	0.048 ± 0.001	1.924 ± 0.033	0.123 ± 0.001	0.02 ± 0.707	0.03 ± 0.0707	1.481 ± 0.1
208 Lacrimosa	0.925 ± 0.01	0.031 ± 0.001	1.907 ± 0.052	0.179 ± 0.002	0.017 ± 0.707	0.023 ± 0.0707	1.309 ± 0.1
277 Elvira	0.931 ± 0.01	0.047 ± 0.001	1.889 ± 0.04	0.178 ± 0.002	0.023 ± 0.707	0.019 ± 0.0707	0.789 ± 0.1
352 Gisela	1.038 ± 0.01	0.128 ± 0.001	1.939 ± 0.046	0.364 ± 0.001	0.039 ± 0.707	0.018 ± 0.0707	0.439 ± 0.1
364 Isara	1.014 ± 0.01	0.14 ± 0.002	1.965 ± 0.026	0.346 ± 0.002	0.053 ± 0.707	0.023 ± 0.0707	0.43 ± 0.1
462 Eriphyla	0.932 ± 0.01	0.038 ± 0.001	1.943 ± 0.044	0.185 ± 0.001	0.018 ± 0.707	0.022 ± 0.0707	1.134 ± 0.1
703 Noemi	0.961 ± 0.01	0.141 ± 0.001	1.948 ± 0.025	0.303 ± 0.002	0.047 ± 0.707	0.023 ± 0.0707	0.466 ± 0.1
808 Merxia	0.925 ± 0.01	0.059 ± 0.002	1.912 ± 0.048	0.169 ± 0.001	0.025 ± 0.707	0.034 ± 0.0707	1.229 ± 0.1
913 Otila	0.977 ± 0.01	0.124 ± 0.003	1.933 ± 0.039	0.198 ± 0.004	0.054 ± 0.707	0.022 ± 0.0707	0.435 ± 0.1

Band areas are determined using the trapezoidal method. The errors for this parameter also utilize the methods of C. A. Thomas et al. (2014), which are similar to the band depth error generation. Here we modify each point along the spectrum with the error of the spectrum and a random number generated over the range of [−1, 1]. We calculate the synthetic area using the same trapezoidal function, generating 20,000 synthetic areas. The error is defined as the standard deviation of the synthetic areas. The BAR is the quotient of Band II area to Band I area.

We impose a minimum error on each measurement to account for systematic uncertainties in the measurements, consistent with the approach in C. A. Thomas et al. (2014) and references therein. All the errors in the band parameter tables are quoted with these errors unless the error is larger than that threshold. Band centers have a minimum error of 0.01, band

areas have a minimum error of 0.07, and BAR has a minimum error of 0.1.

The band parameters for each object are presented in Table A1.

A.2. Mineralogy Discussion

A.2.1. Comparison to Literature

As we discussed in Section 2.3, some of the asteroids presented here have been observed previously with a variety of techniques. We will discuss now our mineralogy results that we derive from near-infrared spectroscopy with previously published results.

M. J. Gaffey et al. (1993) presented spectra for a large number of the objects we observed. We report different interpretations of S-type subclass for most of the objects observed in both studies. Beginning with the similarities, we find that five of our interpretations of S-type subclass are consistent with M. J. Gaffey et al. (1993) ((3) Juno, (6) Hebe, (7) Iris, (20) Massalia, and (67) Asia).

Most of the asteroids we interpret differently than M. J. Gaffey et al. (1993) are quite close in parameter space to the M. J. Gaffey et al. (1993) reported band parameters (including (9) Metis, (11) Parthenope, (33) Polyhymnia, (63) Ausonia, (82) Alkmene, (115) Thyra, and (364) Isara). For example, (11) Parthenope in our work is interpreted to be an S(III) subclass object. It appears just leftward of the left of the S(IV) field in the Band I center versus BAR plot. S(IV) subclass was the assignment for Parthenope in M. J. Gaffey et al. (1993). This suggests that differences in observing conditions, observing geometry, signal-to-noise ratio between the observations, advances in instrumentation between this work and that of M. J. Gaffey et al. (1993), or choice of endpoints for the band parameter analysis (e.g., J. A. Sanchez et al. 2020) are the likely cause of these minor differences.

One object, however, is significantly different. Our spectrum of Melpomene is quite different from the one presented in M. J. Gaffey et al. (1993). The difference between our spectrum of Melpomene and the one in M. J. Gaffey et al. (1993) might indicate significant parent-body heterogeneity on this asteroid.

A.3. Potential Parent-body Heterogeneity

We obtained multiple observations of three asteroids, (14) Irene, (17) Thetis, and (182) Elsa. Each observation of the asteroids resulted in a different interpretation of the underlying mineralogy.

Elsa was observed twice (Figure A2), 8 days apart in fall of 2019. Elsa has a very long rotation period (~80 hr), so the elapsed time between the two observations represents ~2.1375 rotations periods. The two prism observations indicate either a basaltic achondrite mineralogy or an S(VI) field mineralogy. The BAR values differ significantly (1.71 ± 0.0061 and 1.50 ± 0.0049, respectively), and the Band I centers are very close in value (0.921 and 0.926 μm). Because Elsa was observed so close in time, the observational circumstances are very similar; the phase angle in particular only changes between the two observations by 0°.6. Given this information, it seems possible that Elsa may have some rotational heterogeneity on its surface. The basaltic achondrite and S(VI) fields are close together in the Gaffey plot parameter space; it seems reasonable that heterogeneity exists on this asteroid.

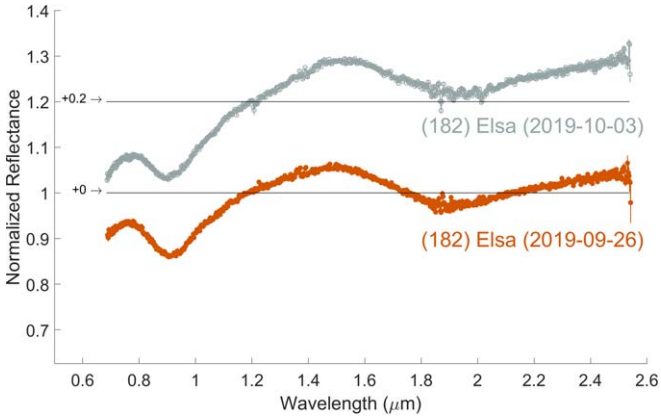

Figure A2. Elsa spectra observed ~1 week apart. Elsa appears to have surface composition heterogeneity.

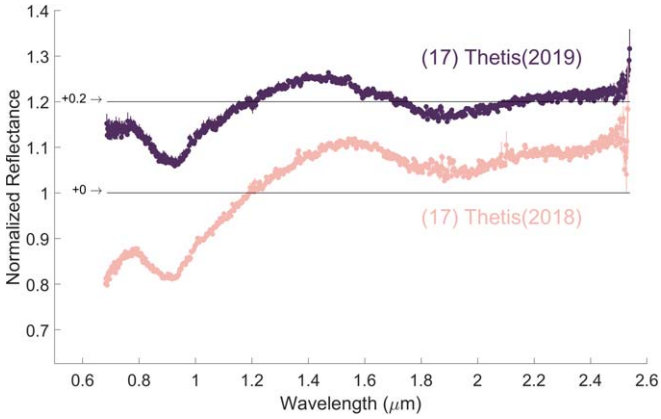

Figure A3. Thetis spectra.

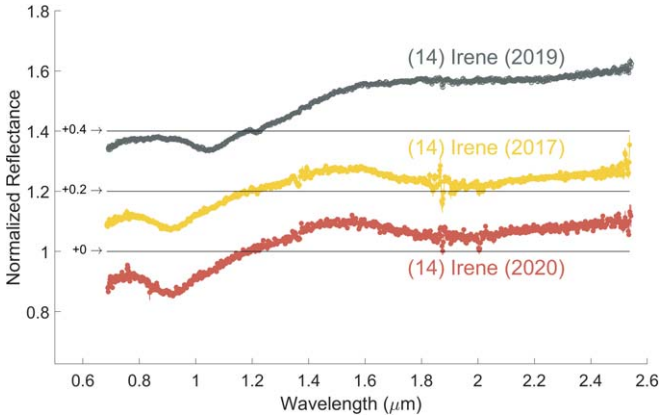

Figure A4. Irene spectra.

Asteroid (17) Thetis (Figure A3) was also observed twice in the course of this project. However, these observations were made ~150 days apart. The second observation was made when the distance between the asteroid and Earth was significantly smaller, and the phase angle was much smaller in the later observation as well. Still, the band parameters are somewhat similar between the two objects: BAR values differ most significantly (1.007 and 1.188); Band I centers are virtually identical (0.926 and 0.926). We interpret the 2019

observation of Thetis to be consistent with a primitive achondrite mineralogy based on the difference between the Band II centers and the observations (1.9 ± 0.053 μm and 1.87 ± 0.038 μm). Further analysis in Appendix B (e.g., Figure B1) shows that the second observation of Thetis is right on the border between the primitive achondrite field and the H chondrite field. The uncertainty on the Band II center could indicate a H chondrite mineralogy. The interpretation of Thetis presented in J. M. Sunshine et al. (2004) indicates the presence of high calcium pyroxene and therefore partial differentiation on this object. The second observation of Thetis is consistent with the finding from J. M. Sunshine et al. (2004). However, grain size and/or space weathering may also affect band parameters by causing subtle changes in an asteroid's spectrum (e.g., Y. Ueda et al. 2002). We conclude that (17) Thetis appears to have rotational heterogeneity. Thetis's surface may have mechanical heterogeneity (e.g., grain size differences), relative difference of surface age, or potentially a compositional difference with some parts of the surface showing evidence of partial differentiation. More observations are needed to confirm this heterogeneity and its cause.

(14) Irene was observed on three separate occasions during data collection (Figure A4), once in each of the following years: 2017, 2019, and 2020. Looking at the spectra, it seems that Irene has three distinct mineralogies, an H-ordinary-chondrite-like spectrum (2020), an intermediate mineralogy (2017), and a basaltic achondrite mineralogy (2019), on the same asteroid. Further investigations of this potential heterogeneity are necessary.

Appendix B
Identifying Asteroids Compositionally Similar to Ordinary Chondrite Subtypes

Studies of ordinary chondrites show that each ordinary chondrite subtype (H, L, and LL) has highly clustered geochemical and petrologic signatures (e.g., total iron abundance, distribution of iron between metal and silicates, disparate clasts, oxygen isotopes; e.g., R. T. Dodd 1981). These clustered signatures allow ordinary chondrites to be categorized into different subtypes. The interpretation of these multiple subtypes in the ordinary chondrite group is that each ordinary chondrite subtype could have formed on a single parent body. Given what we know of planet formation, it is more likely that ordinary chondrite subtype groups are sourced from populations of asteroids that formed very close in time and space to each other such that their initial chemical compositions, including short-lived radioactive nuclei abundance, were similar (e.g., J. A. Wood 2005). As a consequence of these similar initial formation conditions, these groups of objects experienced similar parent-body evolution, resulting in a population of meteorites that are petrologically identical even if not sourced from the exact same object.

Using the methodologies in T. L. Dunn et al. (2010) and J. A. Sanchez et al. (2020), we can determine the similarity between the ordinary-chondrite-like asteroids with each of the three subtypes. First, it is necessary to investigate whether any of the objects in this study are related to primitive achondrites that can plot in the same region as ordinary chondrites in the Gaffey plot.

M. P. Lucas et al. (2019) showed that acapulcoite−lodranite clan meteorites plot in the S(IV) parameter space on the Gaffey plot, yet they are compositionally distinct from ordinary chondrites. It appears that the acapulcoite−lodranite clan meteorites formed from a chondritic precursor and then experienced heating to the point of silicate melting. These parent bodies did not experience full differentiation but rather partial melting that affected the textures and compositions of the precursor materials. The acapulcoite−lodranite clan meteorites come from parent bodies distinct from the ordinary chondrites. Ordinary chondrites experienced heating, resulting in thermal metamorphism evident in the textures and composition of these meteorites.

M. P. Lucas et al. (2019) show that the acapulcoite−lodranite clan meteorites are distinct from ordinary chondrites in the Band I center versus Band II center parameter space. The

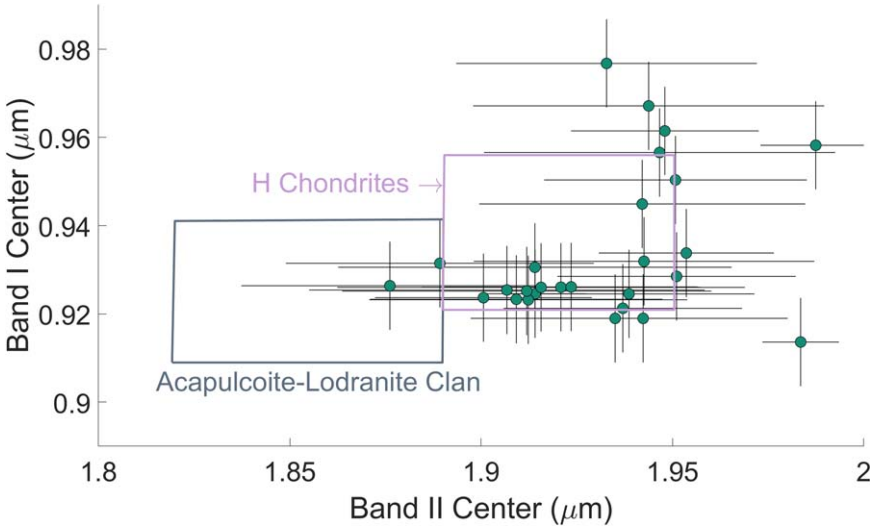

Figure B1. Band I center vs. Band II center for the S-type asteroids observed. This plot is based on the work of M. P. Lucas et al. (2019), where primitive achondrites in the acapulcoite−lodranite clan can be distinguished from H ordinary chondrites. Both groups of meteorites appear in the ordinary chondrite boot of the M. J. Gaffey et al. (1993) plot. Using the Band I vs. Band II centers allows us to distinguish any asteroids that may have experienced partial melting. We find two potential acapulcoite−lodranite clan asteroids: (277) Elvira and (17) Thetis (2018). The Thetis band centers are on the boundary with H ordinary chondrites but still may represent unequilibrated and partially melted lithologies on the same object.

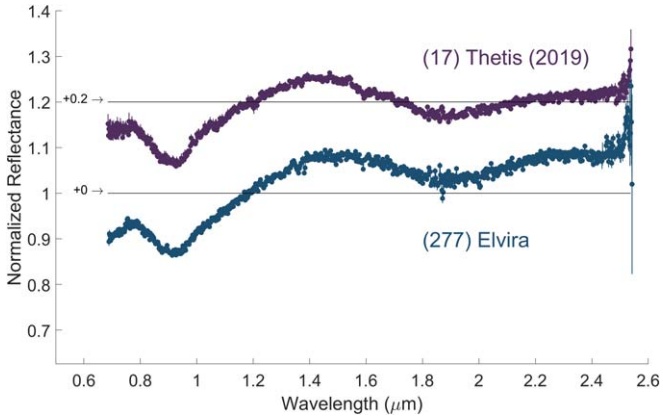

Figure B2. Acapulcoite−lodranite-like asteroids. (17) Thetis (observed in 2019) and (277) Elvira are spectrally consistent with the partially melted achondrites in the acapulcoite−lodranite clan (M. P. Lucas et al. 2019). This indicates that these objects might not be ordinary-chondrite-like but might represent asteroids that experienced different parent-body processing.

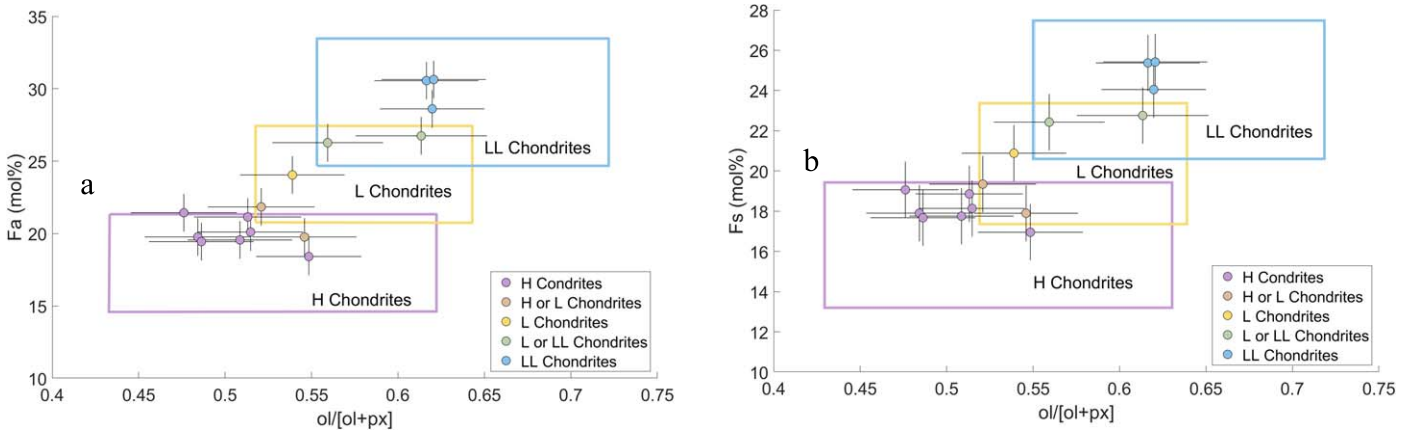

Figure B3. (a) Abundance of olivine vs. fayalite abundance derived from band parameter analysis. (b) Abundance of olivine vs. ferrosilite abundance. Asteroids that plot in the ordinary chondrite boot are compared to their relative abundance of fayalite, ferrosilite, and total olivine based on the analysis of T. L. Dunn et al. (2010), with the refinements of the original empirical relationships for mineralogy from J. A. Sanchez et al. (2020). We see that the ordinary-chondrite-like asteroids have similarities to H, L, and LL chondrites. The subtyping of the asteroids is listed in Tables 4 and 5.

acapulcoite−lodranite clan meteorites exhibit lower ferrous iron content in both the olivines and pyroxenes present compared to H ordinary chondrites. This compositional difference reveals itself in the Band I center versus Band II center parameter space, where H chondrites have Band II centers at longer wavelengths compared to the less iron-rich acapulcoite−lodranite clan meteorites. Similarly, the Band I centers for H chondrites are at a slightly longer wavelength again owing to the iron content compared to acapulcoite −lodranite clan meteorites.

Considering this parameter space for our asteroids (Figure B1), we find that two of the S(IV) objects plot in the lower-iron region in the Band I center versus Band II center, indicating that these objects, (277) Elvira and (17) Thetis (observed in 2019), are likely partially melted primitive achondrites rather than ordinary chondrites. Their spectra are presented in Figure B2. However, particle size and space weathering can subtly shift band parameters (e.g., Y. Ueda et al. 2002). Without any a priori knowledge about the surface age or grain size on the surfaces of the two potential acapulcoite−lodranite-like asteroids, and given the relative size of the error on the measurements, it is possible that both (277) Elvira and (17) Thetis are consistent with H ordinary chondrite mineralogy. We exclude them from the remaining analysis out of an abundance of caution.

Taking the remaining 15 objects that are likely ordinary-chondrite-like (rather than achondritic), we now attempt to determine the subtype of each asteroid.

In their systematic spectral-mineralogical study, T. L. Dunn et al. (2010) show that abundance of olivine (ol/ol+px) and the relative abundance of fayalite and ferrosilite can be derived using Band I/II centers and areas. When the derived olivine and ferrosilite/fayalite abundances are plotted, each ordinary chondrite subclassification can be distinguished. We will describe how each of these quantities is derived and present our analysis of these data.

T. L. Dunn et al. (2010) provide empirical relationships based on band parameters and compositions derived through XRD analyses of the ordinary chondrites in their sample. J. A. Sanchez et al. (2020) returned to their analyses but explored how signal-to-noise ratio and wavelength range affect these empirical relationships. Typically, telescopic data do not cover the same wavelength range as laboratory data, and telescopic data have lower signal-to-noise ratio. These so-

Table B1
Ordinary-chondrite-like Asteroids and Modal Mineralogy

Asteroid	ol/ol+px	Modal Abundance of Fayalite	Modal Abundance of Ferrosilite	Subtype Designation
3 Juno	0.56 ± 0.03	26.27 ± 1.3	22.43 ± 1.4	L or LL
5 Astrea	0.48 ± 0.03	19.77 ± 1.3	17.90 ± 1.4	H
6 Hebe	0.51 ± 0.03	21.15 ± 1.3	18.86 ± 1.4	H
7 Iris	0.62 ± 0.03	30.56 ± 1.3	25.37 ± 1.4	LL
14 Irene (2020)	0.55 ± 0.03	18.42 ± 1.3	16.95 ± 1.4	H
(17) Thetis (2018)	0.51 ± 0.03	20.11 ± 1.3	18.14 ± 1.4	H
30 Urania	0.54 ± 0.03	24.05 ± 1.3	20.88 ± 1.4	L
67 Asia	0.49 ± 0.03	19.45 ± 1.3	17.68 ± 1.4	H
82 Alkmene	0.51 ± 0.03	19.56 ± 1.3	17.75 ± 1.4	H
103 Hera	0.52 ± 0.03	21.85 ± 1.3	19.35 ± 1.4	H or L
115 Thyra	0.55 ± 0.03	19.77 ± 1.3	17.90 ± 1.4	H or L
364 Isara	0.62 ± 0.03	30.64 ± 1.3	25.42 ± 1.4	LL
462 Eriphyla	0.48 ± 0.03	21.44 ± 1.3	19.07 ± 1.4	H
703 Noemi	0.61 ± 0.04	26.75 ± 1.3	22.76 ± 1.4	L or LL
913 Otila	0.62 ± 0.03	28.62 ± 1.3	24.05 ± 1.4	LL

called "incomplete data sets" yield different band parameters than laboratory data, which is related to the wavelength range and signal-to-noise ratio of the observations. Using the updated J. A. Sanchez et al. (2020) empirical relationships that are relevant to the wavelength range of prism data, we determine the olivine−pyroxene abundance ratio and molar content of ferrosilite and fayalite for our objects using these empirical relationships:

$$\frac{\mathrm{ol}}{\mathrm{ol}+\mathrm{px}} = -0.2053 \times \mathrm{BAR} + 0.709,$$

$$\mathrm{Fa} = -1283.4 \times \mathrm{BIC}^2 + 2609.5 \times \mathrm{BIC} - 1295.8,$$

$$\mathrm{Fs} = -904.4 \times \mathrm{BIC}^2 + 1837.3 \times \mathrm{BIC} - 907.7.$$

Here BIC stands for the Band I center position. Plotting the olivine−pyroxene abundance ratio against the modal abundance of fayalite and, separately, the modal abundance of ferrosilite allows us to determine ordinary chondrite subclassification for the asteroids in our data set (Figure B3). We find that a significant fraction of our S(IV) asteroids are consistent with H ordinary chondrite mineralogy (7 of the 15 objects). Two asteroids are consistent with either H or L chondrite mineralogy; one asteroid appears to be L-chondrite-like, while three are LL-chondrite-like. We also have two asteroids that could be either L- or LL-chondrite-like.

The modal mineralogies for the H-ordinary-chondrite-like asteroids are presented in Table B1.

The olivine abundances for the ordinary-chondrite-like asteroids are generally lower in value compared to the abundances derived from visible/near-infrared spectroscopy (Iris, Isara). P. Vernazza et al. (2010) report 76.5% and 77%, respectively, for [ol/ol+px] values comparted 61% ± 3% and 62% ± 3%. This difference may be related to the fact that we do not have visible wavelengths as a part of our analysis. Subtle differences between endpoints and signal-to-noise ratios can change the derived quantities (e.g., J. A. Sanchez et al. 2020). Taking an average value of the P. Vernazza et al. (2010) results based on the derived olivine abundances using all techniques (e.g., visible−near-infrared spectroscopy and two derivations with different mid-infrared observations), our values are roughly consistent with theirs.

The mineralogy of Iris was reported to be LL-ordinary-chondrite-like (J. W. Noonan et al. 2019). Our results are in agreement. Those authors also presented a spectrum and interpretation of (3) Juno. Here our results differ: J. W. Noonan et al. (2019) find June to be similar to H ordinary chondrites. We find Juno to be more consistent with L or LL lithologies. Juno is known to have a heterogenous surface (e.g., J. Degewij et al. 1979; K. Shinokawa et al. 2002) with one likely significant impact crater (S. Baliunas et al. 2003). It is possible that the impact event emplaced material of different composition on the surface, which could result in the observed heterogeneity between this work and that of J. W. Noonan et al. (2019).

ORCID iDs

Cristina Thomas https://orcid.org/0000-0003-3091-5757
Andrew Rivkin https://orcid.org/0000-0002-9939-9976
Joshua Emery https://orcid.org/0000-0001-9265-9475

References

Arredondo, A., McAdam, M. M., Honniball, C. I., et al. 2024, Detection of Molecular H2O on Nominally Anhydrous Asteroids, PSJ, 5, 37
Avdellidou, C., Price, M. C., Delbo, M., Ioannidis, P., & Cole, M. J. 2016, Survival of the Impactor During Hypervelocity Collisions-I. An Analog for Low Porosity Targets, MNRAS, 456, 2957
Baliunas, S., Donahue, R., Rampino, M. R., et al. 2003, Multispectral Analysis of Asteroid 3 Juno taken with the 100-inch Telescope at Mount Wilson Observatory, Icar, 163, 135
Bell, J. F., Davis, D. R., Hartmann, W. K., & Gaffey, M. J. 1989, Asteroids: The Big Picture, Asteroids II, ed. R. P. Binzel, T. Gehrels, & M. S. Matthews (Tucson, AZ: Univ. Arizona Press), 921
Benna, M., Hurley, D. M., Stubbs, T. J., Mahaffy, P. R., & Elphic, R. C. 2019, Lunar Soil Hydration Constrained by Exospheric Water Liberated by Meteoroid Impacts, NatGe, 12, 333
Bottke, W. F., Nolan, M. C., Greenberg, R., & Kolvoord, R. A. 1994, Velocity Distributions Among Colliding Asteroids, Icar, 107, 255
Bowell, E., Chapman, C. R., Gradie, J. C., Morrison, D., & Zellner, B. 1978, Taxonomy of Asteroids, Icar, 35, 313
Broglia, P., Manara, A., & Farinella, P. 1994, Polarimetric Observations of (6) Hebe, Icar, 109, 204
Burbine, T. H., & Binzel, R. P. 2002, Small Main-belt Asteroid Spectroscopic Survey in the Near-infrared, Icar, 159, 468
Campins, H., Hargrove, K., Pinilla-Alonso, N., et al. 2010, Water Ice and Organics on the Surface of the Asteroid 24 Themis, Natur, 464, 1320
Chapman, C. R., & Salisbury, J. W. 1973, Comparisons of Meteorite and Asteroid Spectral Reflectivities, Icar, 19, 507
Clark, Roger N. 2009, Detection of Adsorbed Water and Hydroxyl on the Moon, Sci, 326, 562

Cloutis, E. A., Gaffey, M. J., Smith, D. G., & Lambert, R. S. J. 1990, Metal Silicate Mixtures: Spectral Properties and Applications to Asteroid Taxonomy, JGR, 95, 8323
Cushing, M. C., Vacca, W. D., & Rayner, J. T. 2004, Spextool: A Spectral Extraction Package for SpeX, a 0.8-5.5 micron Cross-dispersed Spectrograph, PASP, 116, 362
De Sanctis, M. C., Combe, J.-P., Ammannito, E., et al. 2012, Detection of Widespread Hydrated Materials on Vesta by the VIR Imaging Spectrometer on Board the Dawn Mission, ApJL, 758, L36
De Sanctis, M. C., Mitri, G., Castillo-Rogez, J., et al. 2020, Relict Ocean Worlds: Ceres, SSRv, 216, 60
Degewij, J., Tedesco, E. F., & Zellner, B. 1979, Albedo and Color Contrasts on Asteroid Surfaces, Icar, 40, 364
Deienno, R., Izidoro, A., Nesvorný, D., & Bottke, W. F. 2023, Size-frequency Distribution of S-complex Implanted Asteroids, in Asteroids Comets Meteors Conf., 2549
DellaGiustina, D. N., Emery, J. P., Golish, D. R., et al. 2019, Properties of Rubble-pile Asteroid (101955) Bennu from OSIRIS-REx Imaging and Thermal Analysis, NatAs, 3, 341
DeMeo, F. E., Binzel, R. P., Slivan, S. M., & Bus, S. J. 2009, An Extension of the Bus Asteroid Taxonomy into the Near-infrared, Icar, 202, 160
Dodd, R. T. 1981, Meteorites: A Petrologic-chemical Synthesis (Cambridge: Cambridge Univ. Press)
Donahue, T. M., & Hodges, R. R. 1993, Venus Methane and Water, GeoRL, 20, 591
Dunham, D. W., & Herald, D. 2006, Asteroid Occultations V4.0. EAR-A-3-RDR-OCCULTATIONS-V4.0, PDSS, https://pds.nasa.gov/ds-view/pds/viewDataset.jsp?dsid=EAR-A-3-RDR-OCCULTATIONS-V4.0
Dunn, T. L., McCoy, T. J., Sunshine, J. M., & McSween, H. Y., Jr 2010, A Coordinated Spectral, Mineralogical, and Compositional Study of Ordinary Chondrites, Icar, 208, 789
Eaton, N., Green, S. F., McCheyne, R. S., Meadows, A. J., & Veeder, G. J. 1983, Observations of Asteroids in the 3- to 4-μm Region, Icar, 55, 245
Gaffey, M. J., Bell, J. F., Brown, R. H., et al. 1993, Mineralogical Variations within the S-type Asteroid Class, Icar, 106, 573
Granahan, J. C. 2011, Spatially Resolved Spectral Observations of Asteroid 951 Gaspra, Icar, 213, 265
Granahan, J. C., Fanale, F. P., Robinson, M. S., et al. 1994, A Galileo Multi-instrument Spectral Analysis of 951 Gaspra, LPSC, 25, 453
Harris, A. W. 1998, A Thermal Model for Near-Earth Asteroids, Icar, 131, 291
Hasegawa, S., Murakawa, K., Ishiguro, M., et al. 2003, Evidence of Hydrated and/or Hydroxylated Minerals on the Surface of Asteroid 4 Vesta, GeoRL, 30, 2123
Hibbitts, C. A., Grieves, G. A., Poston, M. J., et al. 2011, Thermal Stability of Water and Hydroxyl on the Surface of the Moon from Temperature-programmed Desorption Measurements of Lunar Analog Materials, Icar, 213, 64
Ho, T.-M., Jaumann, R., Bibring, J.-P., et al. 2021, The MASCOT Lander Aboard Hayabusa2: the in-situ Exploration of NEA (162173) Ryugu, P&SS, 200, 105200
Honniball, C. I., Lucey, P. G., Arredondo, A., Reach, W. T., & Malaret, E. R. 2022, Regional Map of Molecular Water at High Southern Latitudes on the Moon Using 6 μm Data From the Stratospheric Observatory for Infrared Astronomy, GeoRL, 49, e2022GL097786
Honniball, C. I., Lucey, P. G., Li, S., et al. 2021, Molecular Water Detected on the sunlit Moon by SOFIA, NatAs, 5, 121
Izidoro, A., Deienno, R., Dasgupta, R., & Isella, A. 2023, The Effect of the Solar System Early Dynamical Instability on the Asteroid Belt Implantation, in Asteroids Comets Meteors Conf., 2544
Jones, T. D., Lebofsky, L. A., Lewis, J. S., & Marley, M. S. 1990, The Composition and Origin of the C, P, and D Asteroids: Water as a Tracer of Thermal Evolution in the Outer Belt, Icar, 88, 172
Keil, K., Haack, H., & Scott, E. R. D. 1994, Catastrophic Fragmentation of Asteroids: Evidence from Meteorites, P&SS, 42, 1109
Kelley, M. S., & Gaffey, M. J. 2000, 9 Metis and 113 Amalthea: A Genetic Asteroid Pair, Icar, 144, 27
Landsman, Z. A., Campins, H., Pinilla-Alonso, N., Hanus, J., & Lorenzi, V. 2015, A New Investigation of Hydration in the M-type Asteroids, Icar, 252, 186
Lawrence, D. J., Feldman, W. C., Goldsten, J. O., et al. 2013, Evidence for Water ice Near Mercury's North Pole From MESSENGER Neutron Spectrometer Measurements, Sci, 339, 292
Lucas, M. P., Emery, J. P., Hiroi, T., & McSween, H. Y. 2019, Spectral Properties and Mineral Compositions of Acapulcoite–Lodranite Clan Meteorites: Establishing S-type Asteroid-Meteorite Connections, M&PS, 54, 157
MacLennan, E. 2019, PhD Dissertation, Univ. Tennessee
Malhotra, R., & Wang, X. 2017, Eccentricity Distribution in the Main Asteroid Belt, MNRAS, 465, 4381
Marchis, F., Kaasalainen, M., Hom, E. F. Y., et al. 2006, Shape, Size and Multiplicity of Main-belt Asteroids: I. Keck Adaptive Optics Survey, Icar, 185, 39
Masiero, J. R., Grav, T., Mainzer, A. K., et al. 2014, Main-belt Asteroids with WISE/NEOWISE: Near-infrared Albedos, ApJ, 791, 121
McCord, T. B., Li, J.-Y., Combe, J.-P., et al. 2012, Dark Material on Vesta from the Infall of Carbonaceous Volatile-rich Material, Natur, 491, 83
McGraw, L. E., Emery, J. P., Thomas, C. A., et al. 2022, 3 μm Spectroscopic Survey of Near-Earth Asteroids, PSJ, 3, 243
Migliorini, F., Manara, A., Scaltriti, F., et al. 1997, Surface Properties of (6) Hebe: A Possible Parent Body of Ordinary Chondrites, Icar, 128, 104
Noonan, J. W., Reddy, V., Harris, W. M., et al. 2019, Search for the H Chondrite Parent Body Among the three Largest S-type Asteroids: (3) Juno, (7) Iris, and (25) Phocaea, AJ, 158, 213
O'Brien, D. P., Sykes, M. V., & Tricarico, P. 2011, Collision Probabilities and Impact Velocity Distributions for Vesta and Ceres, LPSC, 42, 2665
Pieters, C. M., Goswami, J. N., Clark, R. N., et al. 2009, Character and Spatial Distribution of OH/H2O on the Surface of the Moon Seen by M3 on Chandrayaan-1, Sci, 326, 568
Prettyman, T. H., Mittlefehldt, D. W., Yamashita, N., et al. 2012, Elemental Mapping by Dawn Reveals Exogenic H in Vesta's Regolith, Sci, 338, 242
Raymond, S. N., & Nesvorny, D. 2022, Origin and Dynamical Evolution of the Asteroid Belt, in Vesta and Ceres. Insights from the Dawn Mission for the Origin of the Solar System, ed. S. Marchi, C. A. Raymond, & C. T. Russell (Cambridge: Cambridge Univ. Press), 227
Rayner, J. T., Toomey, D. W., Onaka, P. M., et al. 2003, SpeX: A Medium-resolution 0.8-5.5 micron Spectrograph and Imager for the NASA Infrared Telescope Facility, PASP, 115, 362
Reddy, V., Le Corre, L., O'Brien, D. P., et al. 2012, Delivery of Dark Material to Vesta via Carbonaceous Chondritic Impacts, Icar, 221, 544
Rivkin, A. S., Davies, J. K., Clark, B. E., Trilling, D. E., & Brown, R. H. 2001, Aqueous alteration on S asteroid 6 Hebe?, LPSC, 32, 1723
Rivkin, A. S., & Emery, J. P. 2010, Detection of Ice and Organics on an Asteroidal Surface, Natur, 464, 1322
Rivkin, A. S., Howell, E. S., Emery, J. P., & Sunshine, J. 2018, Evidence for OH or H2O on the Surface of 433 Eros and 1036 Ganymed, Icar, 304, 74
Rivkin, A. S., Howell, E. S., Lebofsky, L. A., Clark, B. E., & Britt, D. T. 2000, The Nature of M-class Asteroids from 3-μm Observations, Icar, 145, 351
Rivkin, A. S., McFadden, L. A., Binzel, R. P., & Sykes, M. 2006, Rotationally-resolved Spectroscopy of Vesta I: 2–4 μm Region, Icar, 180, 464
Rubin, A. E., & Bottke, W. F. 2009, On the Origin of Shocked and Unshocked CM clasts in H-chondrite Regolith Breccias, M&PS, 44, 701
Sanchez, J. A., Thomas, C., Reddy, V., et al. 2020, A New Method for Deriving Composition of S-type Asteroids from Noisy and Incomplete Near-infrared Spectra, AJ, 159, 146
Sanchez, J. A., Reddy, V., Nathues, A., et al. 2012, Phase Reddening on Near-Earth Asteroids: Implications for Mineralogical Analysis, Space Weathering and Taxonomic Classification, Icar, 220, 36
Shinokawa, K., Takahashi, S., Ogawa, K., et al. 2002, Observations of Photopolarimetric Variation with the Rotation of Asteroids, 3 Juno and 216 Kleopatra, MmSAI, 73, 658
Sunshine, J. M., Bus, S. J., McCoy, T. J., et al. 2004, High-calcium Pyroxene as an Indicator of Igneous Differentiation in Asteroids and Meteorites, M&PS, 39, 1343
Sunshine, J. M., Farnham, T. L., Feaga, L. M., et al. 2009, Temporal and Spatial Variability of Lunar Hydration as Observed by the Deep Impact Spacecraft, Sci, 326, 565
Svetsov, V. 2011, Cratering Erosion of Planetary Embryos, Icar, 214, 316
Takir, D., & Emery, J. P. 2012, Outer Main Belt Asteroids: Identification and Distribution of Four 3-μm Spectral Groups, Icar, 219, 641
Tedesco, E. F., Noah, P. V., Noah, M., & Price, S. D. 2004, IRAS Minor Planet Survey. IRAS-A-FPA-3-RDR-IMPS-V6.0, PDSS, doi:10.26033/PF3K-M168
Thomas, C. A., Emery, J. P., Trilling, D. E., et al. 2014, Physical Characterization of Warm Spitzer-observed Near-Earth Objects, Icar, 228, 217
Ueda, Y., Hiroi, T., Pieters, C. M., & Miyamoto, M. 2002, Changes of Band I Center and Band II/Band I Area Ratio in Reflectance Spectra of Olivine-pyroxene Mixtures due to the Space Weathering and Grain Size Effects, LPSC, 33, 2023
Vacca, W. D., Cushing, M. C., & Rayner, J. T. 2003, A Method of Correcting Near-infrared Spectra for Telluric Absorption1, PASP, 115, 389

Vernazza, P., Carry, B., Emery, J., et al. 2010, Mid-infrared Spectral Variability for Compositionally Similar Asteroids: Implications for Asteroid Particle Size Distributions, Icar, 207, 800
Warner, B. D., Harris, A. W., & Pravec, P. 2021, Asteroid Lightcurve Data Base (LCDB) Bundle V4.0. urn:nasa:pds:ast-lightcurve-database::4.0, PDSS, doi:10.26033/j3xc-3359
Wood, J. A. 2005, The Chondrite types and their Origins, ASP Conf. Ser. 341, Chondrites and the Protoplanetary Disk (San Francisco, CA: ASP), 953
Wordsworth, R. D. 2016, The Climate of early Mars, AREPS, 44, 381
Wray, J. J. 2021, Contemporary Liquid Water on Mars?, AREPS, 49, 141
Yoshikawa, M., Fujiwara, A., Kawaguchi, J., & Mission, H. 2006, The Nature of Asteroid Itokawa Revealed by Hayabusa, in IAU Symp. 236, Near Earth Objects, our Celestial Neighbors, ed. G. B. Valsecchi, D. Vokrouhlický, & A. Milani (Cambridge: Cambridge Univ. Press), 401
Zellner, B. 1979, The Tucson Revised Index of Asteroid Data, Asteroids (Tucson, AZ: Univ. Arizona Press), 1011